Cell Reports
Medicine

Article

Targeting TET3 suppresses group 3 medulloblastoma stemness and progression via impairing hypomethylation of *Otx2* super-enhancer

Graphical abstract

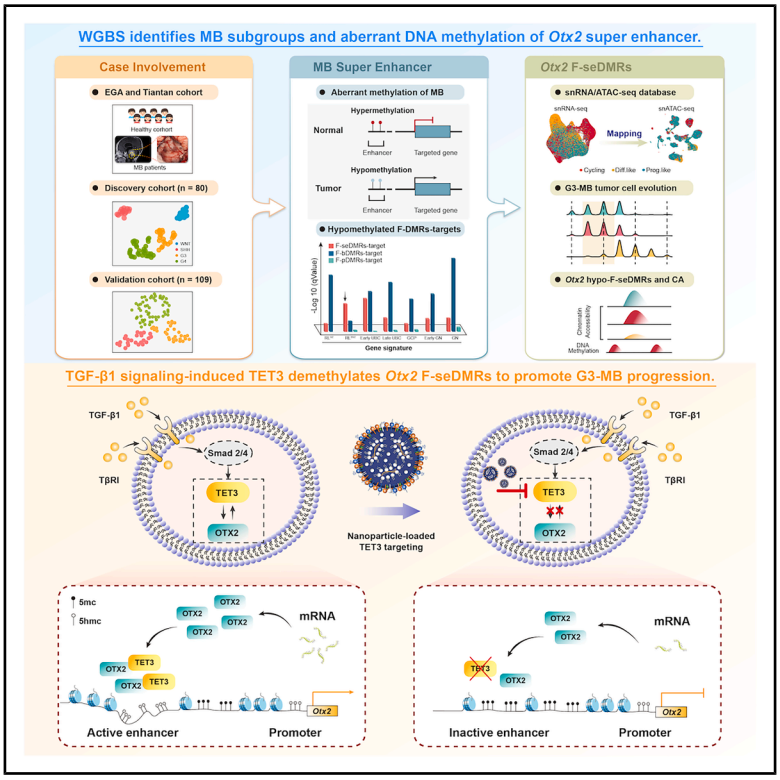

Highlights

- Enhancer hypomethylation sustains stemness and drives progression of G3-MB
- TET3-mediated demethylation of Otx2 super-enhancer reveals therapeutic vulnerability
- LNP delivery of TET3 inhibitors or siRNAs effectively suppresses G3-MB growth

Authors

Xuan Chen, Ziwei Wang, Yan Song, ..., Guo Liang Li, Tao Jiang, Hailong Liu

Correspondence

glli@buct.edu.cn (G.L.L.), zacharytaojiang@163.com (T.J.), liuhailonger@163.com (H.L.)

In brief

Chen et al. identify TET3-mediated hypomethylation of the *Otx2* super-enhancer as a critical driver of G3-MB. Disrupting this axis with LNP-delivered siTET3 effectively suppresses tumor growth, establishing both a mechanistic hallmark and therapeutic vulnerability of G3-MB.

Chen et al., 2025, Cell Reports Medicine 6, 102474
December 16, 2025 © 2025 The Authors. Published by Elsevier Inc.
https://doi.org/10.1016/j.xcrm.2025.102474

CellPress

Cell Reports Medicine

CellPress
OPEN ACCESS

Article

Targeting TET3 suppresses group 3 medulloblastoma stemness and progression via impairing hypomethylation of *Otx2* super-enhancer

Xuan Chen,[1,2,3,29] Ziwei Wang,[2,3,29] Yan Song,[4,29] Yu Su,[5,29] Yahui Zhao,[6,7,8,29] Jiankang Li,[2,3,26,27,29] Wei Wang,[9] Jiao Zhang,[10,11,12,13] Craig Daniels,[10,11,12,13] Xiaochong Wu,[10,11,12,13] Olivier Saulnier,[14] Yanan Wang,[15] Fei Liu,[6,16] Kaiwen Deng,[6,16] Dongming Han,[1,2,3] Zijia Liu,[1,2,3] Meiyu Li,[1,2,3] Liam D. Hendrikse,[12,13]

(Author list continued on next page)

[1]College of Life Sciences, University of Chinese Academy of Sciences, Beijing 100049, China
[2]BGI Research, Chongqing 401329, China
[3]BGI Research, Shenzhen, Guangdong 518083, China
[4]State Key Laboratory of Chemical Resource Engineering, Beijing University of Chemical Technology, Beijing 10029, China
[5]School of Public Health, Capital Medical University, Beijing 100069, China
[6]Department of Neurosurgery, Beijing Tiantan Hospital, Capital Medical University, Beijing 100070, China
[7]China National Clinical Research Center for Neurological Diseases, Beijing Tiantan Hospital, Capital Medical University, Beijing 100070, China
[8]Beijing Neurosurgical Institute, Beijing 100070, China
[9]Laboratory of Tumor Immunology, Beijing Pediatric Research Institute, Beijing Children's Hospital, Capital Medical University, National Center for Children's Health, Beijing 100045, China
[10]Cancer and Hematology Center, Texas Children's Hospital, Houston, TX 77002, USA
[11]Department of Pediatrics–Hematology/Oncology and Neurosurgery, Baylor College of Medicine, Houston, TX 77002, USA
[12]The Arthur and Sonia Labatt Brain Tumor Research Centre, The Hospital for Sick Children, Toronto, ON M5G 1, Canada
[13]The Developmental and Stem Cell Biology Program, The Hospital for Sick Children, Toronto, ON M5G 1, Canada
[14]Genomics and Development of Childhood Cancers Lab, Inserm U1330, Institut Curie, PSL University, SiREDO Oncology Center, Paris, France
[15]State Key Laboratory of Common Mechanism Research for Major Diseases, Department of Physiology, Institute of Basic Medical Sciences and School of Basic Medicine, Chinese Academy of Medical Sciences and Peking Union Medical College, Beijing 100730, China
[16]Department of Radiotherapy, Beijing Tiantan Hospital, Capital Medical University, Beijing 100070, China
[17]Department of Medical Biophysics, University of Toronto, Toronto, ON M5G 1, Canada

(Affiliations continued on next page)

SUMMARY

Medulloblastoma (MB), particularly Group_3 (G3-MB), remains the most aggressive subgroup due to strong stemness and therapeutic resistance. Through genome-wide DNA methylation and transcriptomic analysis of human MB samples, we identify enhancer hypomethylation as a key feature sustaining G3-MB stemness and tumor progression. Notably, hypomethylation of the *Otx2* super-enhancer (SE) is a prognostic marker and potential therapeutic target for G3-MB patients. We demonstrate that disrupting *Otx2* SE activity effectively reduces tumor growth *in vivo*, highlighting its critical role in G3-MB maintenance. TET3, recruited by OTX2, demethylates the *Otx2* SE, promoting chromatin opening and sustaining tumor proliferation and stemness. To translate these findings into therapy, we develop a liposomal nanoparticle (LNP)-based delivery system for siTET3 or a cytosine-based inhibitor of TET3, achieving significant tumor-suppressive effect in a patient-derived orthotopic xenograft model of G3-MB. Our study provides the targeted approach for *Otx2*-driven G3-MB and introduces LNP-based epigenetic therapy as a promising low-toxicity strategy.

INTRODUCTION

Medulloblastoma (MB) accounts for approximately 25% of childhood brain malignancies,[1] which has been classified into four subgroups, including WNT, SHH, Group_3 (G3-MB), and Group_4 (G4-MB).[2,3] G3-MB patients suffer from a high metastasis rate and the poorest prognosis, with a 5-year survival rate of less than 50%.[1] Recent studies show that MBs with high

This is an open access article under the CC BY-NC-ND license (http://creativecommons.org/licenses/by-nc-nd/4.0/).

Alexandra Rasnitsyn,[12,13,17] Evan Y. Wang,[12,13] Dongyang Wang,[6] Zhaoyang Feng,[6,16] Yanong Li,[16] Zitong Zhao,[18] Hongyu Yuan,[19] Youliang Sun,[19] Yifei Jiang,[20,21] Yanfeng Shi,[7] Tao Yang,[22] Xueling Qi,[23] Yong Hou,[1,3] Chunde Li,[6] Yong-qiang Liu,[24] Yu Tian,[5,25] Shuaicheng Li,[26] Xiaoguang Qiu,[17] Michael D. Taylor,[10,11,12,13] Guo Liang Li,[4,*] Tao Jiang,[6,7,8,*] and Hailong Liu[7,8,16,28,30,*]

[18]State Key Laboratory of Molecular Oncology, National Cancer Center/Cancer Hospital, Chinese Academy of Medical Sciences and Peking Union Medical College, Beijing 100021, China
[19]Institute of Basic Medicine, School of Medicine, Tsinghua University, Beijing 100084, China
[20]University of Michigan-Shanghai Jiao Tong University Joint Institute, Shanghai Jiao Tong University, Shanghai 200240, China
[21]Department of Biomedical Engineering, University of Michigan, Ann Arbor, MI 48109, USA
[22]China National GeneBank, BGI-Research, Shenzhen, Guangdong 518083, China
[23]Department of Neuro-Pathology, Sanbo Brain Hospital Capital Medical University, Beijing 100093, China
[24]Research Center of Chinese Herbal Resource Science and Engineering, School of Pharmaceutical Sciences, Guangzhou University of Chinese Medicine, Guangzhou, Guangdong 510006, China
[25]Division of Cancer Epidemiology, German Cancer Research Center (DKFZ), Heidelberg, Germany
[26]Computer Science Department, City University of Hong Kong, Kowloon, Hong Kong, China
[27]State Key Laboratory of Genome and Multi-omics Technologies, BGI Research, Shenzhen 518083, China
[28]Chinese Institute for Medical Research, Beijing 100069, China
[29]These authors contributed equally
[30]Lead contact
*Correspondence: glli@buct.edu.cn (G.L.L.), zacharytaojiang@163.com (T.J.), liuhailonger@163.com (H.L.)
https://doi.org/10.1016/j.xcrm.2025.102474

cellular plasticity are prone to distant dissemination.[4] G3-MB originates from progenitor cells in the developing human cerebellar rhombic lip subventricular zone (RL^{SVZ}),[5] which endows it with robust stem-like properties contributing to therapy resistance.[6] Current treatment mainly relies on radio-chemotherapy after surgery. However, intensified therapy causes irreversible neurological damage in young patients. Therefore, it is crucial to develop novel therapeutic strategies to improve the current treatment outcomes, which necessitates a deeper understanding of the mechanisms of tumor cell fate determination.

Recent advances in targeted therapies have shown promise in MB subgroups. WNT and SHH pathway inhibitors have demonstrated efficacy against WNT-MB and SHH-MB in preclinical studies.[7,8] However, for G3-MB, which is primarily driven by epigenetic dysregulation, the development of targeted therapies remains challenging due to the lack of druggable driver mutations.[9] Epigenetic targeting has emerged as a promising approach for G3-MB, where dysregulated super-enhancers (SEs) sustain stem-like properties and confer therapy resistance. BET inhibitors (BETi,; bromodomain and extra-terminal inhibitors), which target BRD4 and block its binding to H3K27ac-marked enhancers, have been shown to effectively suppress MYC-driven G3-MB.[10] Similarly, HDAC (histone deacetylase) inhibitors disrupt SE function by preventing histone deacetylation, leading to chromatin remodeling and destabilization of MYC-driven transcriptional programs.[11,12] However, current therapeutic efforts have largely focused on *MYC*-driven tumors, while treatment strategies targeting OTX2-activated G3-MB remain unexplored.

SEs, dense cluster of enhancers critical for regulating cell identity and function, playing a pivotal role in determining cell fate during developmental stages, have been implicated in MB.[13] Moreover, they are enriched with specific transcription factors (TFs) and consequently influence gene expression. Perturbation of SEs impacts MB transcriptional program, highlighting their potential for therapeutic targeting.[14,15] Precise epigenetic mechanisms governing distal *cis*-regulatory regions remain incompletely understood. DNA demethylation, catalyzed by ten-eleven translocation (TET) family, is positively correlated with active SEs and open chromatin.[16] Several differentially demethylated SEs targeting nearby oncogenes have been recently identified.[17] Orthodenticle homeobox 2 (OTX2) is a primary regulator of cell fate determination in G3-MB, and its transcriptional activation promotes self-renewal and maintains the characteristics of primitive RL progenitor cells, thereby hindering differentiation.[5,18] Previous study has found that OTX2 reshaped enhancer chromatin activity to control tumor cell survival and growth.[19] However, it is still unclear whether dynamic methylation in *Otx2* SEs affects gene activation. Additionally, to develop the therapy targeting the regulation of *Otx2*, the mechanisms controlling demethylation and its impact on G3-MB pathogenesis require further clarification.

By integrating whole-genome bisulfite sequencing (WGBS) and bulk RNA sequencing (RNA-seq) data from 189 human MB samples, we uncovered a critical role for enhancer hypomethylation in maintaining the stem-like state of G3-MB progenitor-like tumor cells. Notably, we identified TET3 as a key regulator of OTX2-driven enhancer hypomethylation, facilitating an autoregulatory loop that reinforces OTX2 expression. Given its role in sustaining oncogenic transcriptional programs, TET3 represents a potential therapeutic target in G3-MB. To validate this, we developed liposome nanoparticle (LNP)-loaded siTET3 and Bobcat339, both of which significantly suppressed tumor growth in cerebellar allograft G3-MB models. This study provides the targeted strategy for OTX2-activated G3-MB and introduces LNP-based delivery as a low-toxicity approach for epigenetic therapy, offering a promising avenue for more effective and safer treatment.

RESULTS

Integrated epigenomic and transcriptomic analysis recapitulated MB subgroups

High-resolution WGBS was performed on 189 treatment-naive MB samples, with 80 cases allocated to discovery cohort and

CellPress
OPEN ACCESS

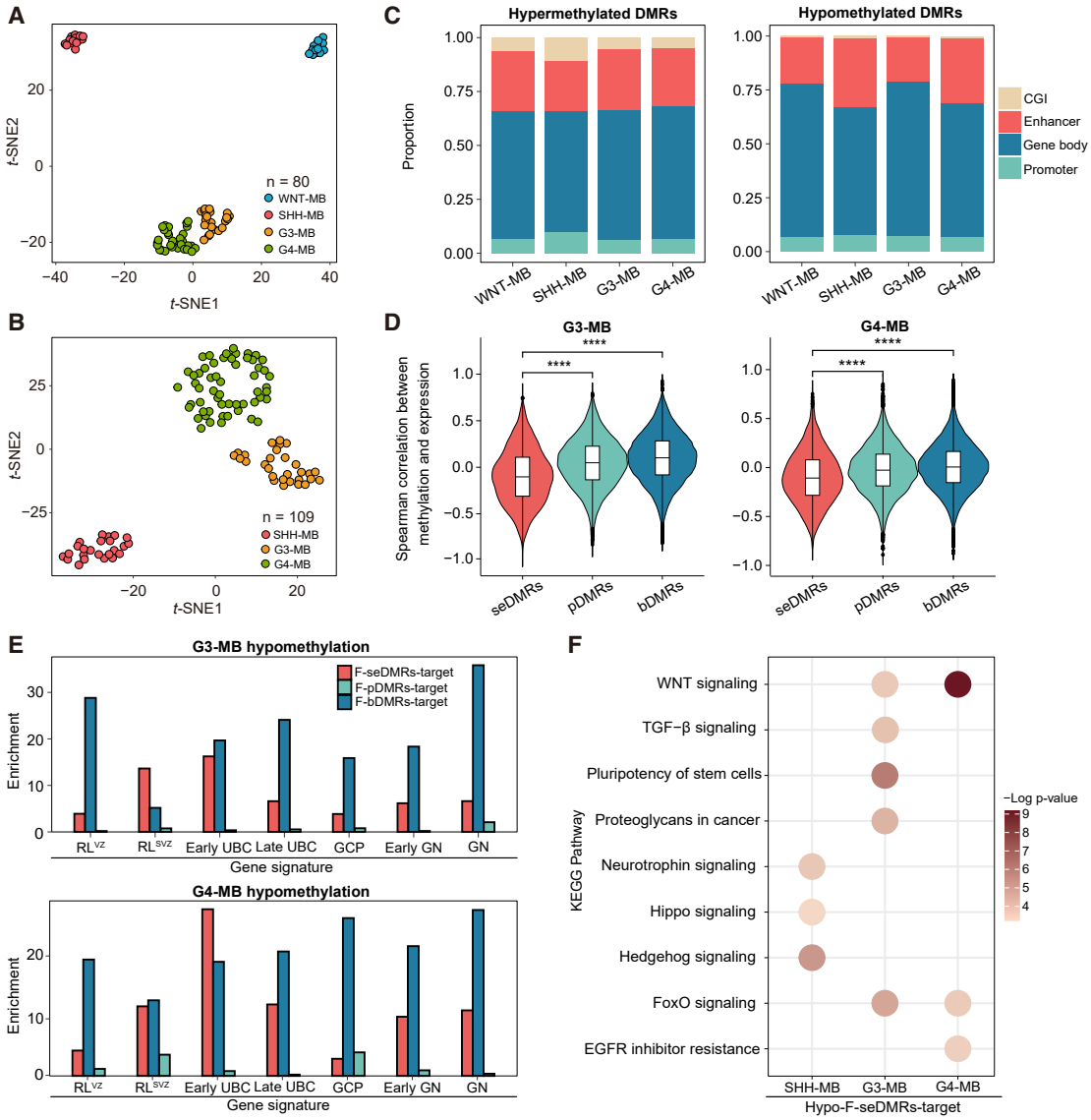

Figure 1. F-seDMR (functional super enhancer differentially methylated region)-targeted genes were related to early cerebellum development signatures

(A) *t*-SNE plots showing the 80 MB samples in the discovery cohort annotated by molecular subgroup based on whole-genome bisulfite sequencing (WGBS) profiles.

(B) *t*-SNE plots showing the 109 MB samples in validation cohort clustered by molecular subgroup based on the identified DMRs as shown in (Figure S1B).

(C) Bar plots showing the proportions of hypermethylated (left) and hypomethylated (right) DMRs across the gene regions. CGI, CpG island.

(D) Violin plots showing the Spearman correlations between DNA methylation and gene expression in DMRs of super-enhancer (seDMRs), promoter (pDMRs), and gene body (bDMRs) in G3-MB and G4-MB; *$p < 0.05$, **$p < 0.01$, ***$p < 0.001$, and ****$p < 0.0001$; two-tailed Mann-Whitney U test.

(E) Bar plots showing the enrichment of hypomethylated F-DMR-targeted genes associated with early-stage developing cerebellar cell types in G3-MB and G4-MB (Fisher's exact test < 0.05). F-DMRs at gene regions: red, F-eDMRs; blue, F-bDMRs; green, F-pDMRs. RL^{VZ}, rhombic lip ventricular zone; RL^{SVZ}, rhombic lip subventricular zone; UBC, unipolar brush cell; GCP, granular cell precursor; GN, granule neuron.

(F) Kyoto Encyclopedia of Genes and Genomes analysis showing the pathways enriched by the Hypo-F-seDMR-targeted marker genes in SHH-MB, G3-MB, and G4-MB.

109 samples in validation cohort (Table S1). The average read depth of CpG sites was calculated at 16.38 coverage, meeting recommended sequencing depth.[20] Subsequent unsupervised clustering of MB cases successfully identified four distinct subgroups in the discovery and validation cohort (Figures 1A and 1B; Table S1). We observed a bimodal distribution of DNA methylation at CpG sites, with complete methylation detected at the vast majority of sites (Figure S1A), akin to previous reports in human brain.[21] The subgroup-specific differentially methylated regions (DMRs) identified from the discovery dataset were employed for

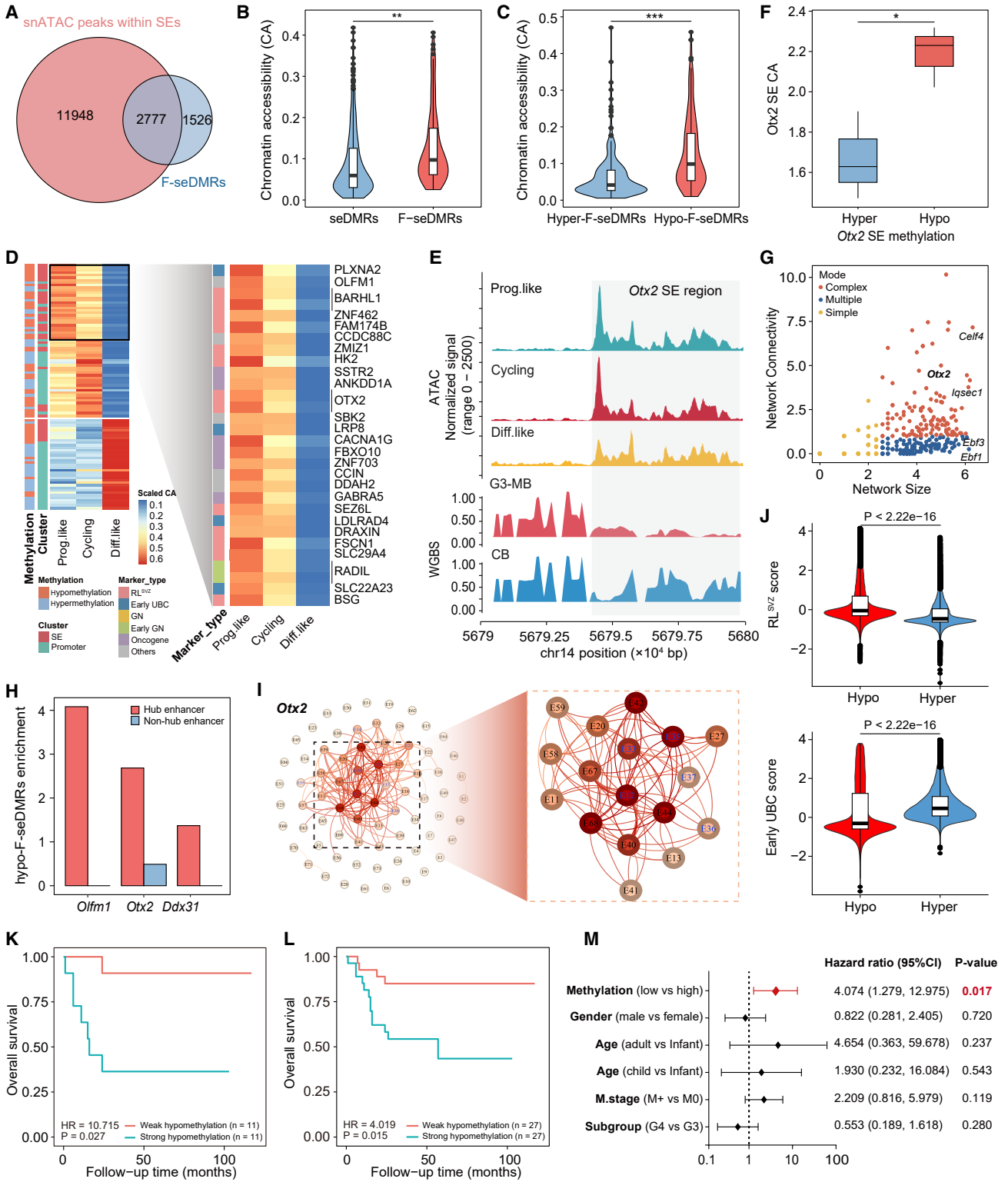

Figure 2. Hypomethylation of *Otx2* hub enhancer as prognostic indicator in G3/4-MB

(A) Venn diagram showing the overlap between snATAC-seq-identified peaks and F-seDMRs in G3-MB.

(B) Violin plot showing the levels of chromatin accessibility (CA) in the seDMRs and F-seDMRs. *$p < 0.05$ and **$p < 0.01$; two-tailed Mann-Whitney U test.

(C) Violin plot showing the CA level in the hyper-F-seDMRs and hypo-F-seDMRs. *$p < 0.05$, **$p < 0.01$, and ***$p < 0.001$; two-tailed Mann-Whitney U test.

(legend continued on next page)

hierarchical clustering of the validation dataset, demonstrating the stability of DMRs-based subgrouping (Figures S1B and S1C; Table S2). Furthermore, subgroup-specific marker genes exhibited altered methylations at these DMRs, suggesting that methylation plays a crucial role in regulating subgroup-specific characteristics (Figure S1D). Additionally, copy-number variation (CNV) analysis demonstrated that DMR-based subgrouping was consistent with the canonical CNVs previously reported for each subgroup, such as chr6-in WNT-MB, chr9q-/chr10q-in SHH-MB, and i17q in G3/4-MB[22] (Figures S1E and S1F).

To elucidate the regulatory role of subgroup-specific DMRs on gene expression, we employed bulk transcriptomics data (n = 169) and identified that DMR-targeted genes exhibited subgroup-specific expression patterns by showing the top 20 differentially expressed genes (Figure S1G). Generally, gene silencing was highly linked to methylated focal regions.[23] We found that several TFs important for each subgroup showed hypomethylation at promoter downstream correlating regions, potentially activating their genes (Figure S1H), consistent with previous reports.[24] Thus, subgroup-specific DMRs underpinned distinct transcription of MB, emphasizing DNA methylome's roles in pathogenesis.

SE DNA hypomethylation was associated with MB tumorigenesis

To delineate the preference for where aberrant methylation occurred, we defined DMRs situated in SE (seDMRs), promoter (pDMRs), gene body (bDMRs), and CpG islands (CGI-DMRs).[25] In the discovery cohort, we examined the distribution of DMRs across genomic elements. Notably, SEs exhibited a prevalence of DMRs across four subgroups, suggesting potential dysregulation of SEs (Figure 1C). We calculated potential associations between DMRs and targeted gene expression based on patient-matched methylation and RNA-seq data. Compared with pDMRs and bDMRs, the seDMR-targeted genes presented a more pronounced negative correlation with methylation (Figures 1D and S2A). Moreover, in G3-MB, aberrant methylation of seDMRs resulted in stronger negative regulation than pDMRs and bDMRs (Figure S2B). Notably, certain genes affected by hypomethylation of seDMRs were subgroup-specific genes (Figure S2C). These findings suggested that seDMRs substantially affected MB-specific gene expression.

MB develops due to failed RL differentiation, causing progenitor cells to stagnate at different lineages and form distinct subgroups.[26,27] SE activity is essential for cellular identity, and its aberrant methylation may disrupt cerebellar markers linked to MB tumorigenesis. Referring to known hallmarks of human embryonic cerebellum,[28,29] via defining as DMRs with Spearman rho < 0 and $p < 0.05$, we found that genes targeted by hypomethylated functional seDMRs (hypo-F-seDMRs), but not the hypermethylated, were significantly enriched in subgroup-originating cerebellar progenitors (Figures 1E and S2D). Furthermore, the targeted genes were also enriched in pathways associated with tumor self-renewal capabilities (Figure 1H). Additionally, the F-seDMR-targeted embryonic cerebellum markers could successfully distinguish G3 and G4 subgroup (Figure S2E), the diagnosis of which has been historically limited to inadequate markers. Collectively, these results suggested that aberrant SEs methylation maintained the progenitor transcriptional characteristics of MB.

Progenitor-like tumor cell-specific SE hypomethylation increased chromatin accessibility in G3-MB

As DNA methylation influences transcriptional programs by altering chromatin organization,[30] we aimed to quantify the chromatin accessibility (CA) in G3-MB through snATAC-seq (single-nucleus assay for transposase-accessible chromatin sequencing) on 76,603 tumor cell nuclei from 8 samples (Table S1). We detected that around 65% of F-seDMRs were located in accessible chromatins (Figure 2A). To explore the relationship between CA and SEs methylation, we focused on these overlapping sites and subsequently found that F-seDMRs presented higher CA levels than did seDMRs (Figure 2B), with hypo-F-seDMRs showing even greater CA than hyper-F-seDMRs (Figure 2C). Despite the considerable variability within the same set of chromatin regions, hypo-F-seDMRs showed consistently greater CA in G3-MB, orchestrating transcriptional programs.

To characterize the heterogeneity of G3-MB, we performed snRNA-seq (single-nucleus RNA sequencing) analysis on 97,801 malignant nuclei from 9 samples (Table S1). Unsupervised clustering of individual cell transcriptomes and visualization through uniform manifold approximation and projection revealed three distinct clusters (Figures S3A and S3B). Based on the previous

(D) Left, heatmap showing the CA levels at SE and promoter regions of three MB tumor cell populations. Right, heatmap showing the CA levels of representative genes with hypo-F-seDMRs in three cell populations.
(E) Top, genome browser track plots showing the CA around *Otx2* hypo-F-seDMRs in three cell populations analyzed by snATAC-seq. Bottom, intermediate 5mC of individual CpGs at enhancers of G3-MB and cerebellum (CB) analyzed by WGBS.
(F) Boxplot showing the CA levels in the hypermethylation or hypomethylation subsets of *Otx2* SE; $^{*}p < 0.05$; two-tailed Mann-Whitney U test.
(G) Scatterplot showing the network size and connectivity of modes. Modes include the complex, multiple, and simple. The top 5 genes ranked by network connectivity and size are labeled.
(H) Bar plot showing the enrichment of hypo-F-seDMRs at "hub enhancers" or "non-hub enhancers" of *Olfm1*, *Otx2*, and *Ddx31* genes.
(I) Node plot showing the *Otx2* enhancer network in G3-MB. The color-coded nodes represent the hypomethylated enhancers, and the empty nodes represent the closed enhancers. The edges indicate the predicted enhancer interactions. The color indicates the connectivity level.
(J) Violin plots showing the expression scores of RL^{SVZ} and early UBC-associated gene signatures in G3-MB tumor cell subset according to the *Otx2* hypo- and hyper-F-seDMRs; two-tailed Mann-Whitney U test.
(K) Kaplan-Meier analysis of overall survival in G3-MB cases subgrouped by strong and weak hypomethylation of *Otx2* F-seDMRs.
(L) Kaplan-Meier analysis of overall survival in G3/4-MB cases subgrouped by the strong and weak hypomethylation of *Otx2* F-seDMRs.
(M) Forest plot showing the HRs for *Otx2* hypo-F-seDMRs in patients with G3-MB and G4-MB as predicted by a Cox proportional hazards model. 95% confidence interval.

study,[31] expression patterns of canonical markers associated with reported cell types revealed three distinct cell lineages: progenitor-like (prog.like), cycling, and differentiation neuronal like (diff.like) tumor cells (Figures S3C and S3E). Pseudo-time analysis revealed a sequential differentiation trajectory of tumor cells, reflecting the development from $RL^{VZ/SVZ}$ toward unipolar brush cell (UBC) and granular neuron (GN).[3,32] Prog.like transcriptomes shared high similarity with those of RL^{SVZ} precursors, whereas more differentiated populations aligned with late-stage cerebellar cell types, such as late UBC, shedding light on evolutionary course (Figure S3D).

We then investigated whether SEs with abnormal hypomethylation showed high CA in the tumor early stage by identifying differentially accessible peaks specific to cell types (Table S3). Most peaks (63%, 19/30) in prog.like (early) tumor cells were situated within hypomethylated SEs. In contrast, a majority of peaks (58%, 21/36) in diff.like (late) tumor cells were located in hypermethylated promoters, with only a small fraction (22%, 8/36) located in hypomethylated SEs (Figures 2D and S3F). In line with these observations, *Otx2* SEs hypomethylation was closely correlated with concomitantly increased CA at MB onset stage (Figures 2D and 2E), as reported by a previous study regarding the effects of *Otx2* on maintaining self-renewal.[18] The association was also observed in other RL^{SVZ}-specific genes, notably *Barhl1* and *Neurog1*[32] (Figure S3G). To corroborate the link between Otx2 SE hypomethylation and stem-like properties, G3-MB patients were dichotomized at the median methylation of *Otx2* SEs. Gene set enrichment analysis revealed that the late UBC/GN differentiation signature was significantly depleted in the hypomethylated group (normalized enrichment score, NES = −1.23, $p = 0.03$; Figure S3H), supporting a model in which hypomethylated *Otx2* SEs suppress the terminal differentiation program and sustain a less differentiated, progenitor-like state associated with stemness.

Hypomethylation of *Otx2* hub enhancer served as a prognostic indicator

Given that hypo-F-seDMRs negatively correlated to gene expression, we next explored how it affected the transcriptional program. The snATAC peaks were utilized to define transcriptionally active SE regions as SE units. The eNET algorithm was then applied to construct enhancer interaction networks for SE units and their respective genes[33,34] (Figure S4A; Table S4A). The accounts and connectivity of modes in each enhancer network were conjointly evaluated, which revealed three distinct modes: complex, multiple, and simple. Higher-ranked genes, sharing the most interactions within the largest networks, like *Celf4* and *Otx2*, were predicted key factors for cell identity and disease according to eNET algorithm[32,33] (Figure 2G).

"Hub enhancers" are characterized by a relatively high frequency of chromatin interactions within targeted genes,[35] which differ from SEs that coordinately regulate gene expression. We then investigated whether hypomethylation within "hub enhancers" impacted transcription. Hypo-F-seDMRs were significantly enriched in "hub enhancers" of three genes, namely, *Otx2*, *Olfm1*, and *Ddx31*, requiring more accessible chromatin cues[33,34] (Figure 2H; Figure S4B). Particularly, extensive "hub enhancer" network interactions were involved in *Otx2* (Figure 2I), and several core regions (blue labeling) in the network showed obvious hypomethylation (Figure 2I; Table S4A). High transcriptional activation of *Otx2*, well documented in G3-MB, has been suggested.[36] Immunohistochemical staining confirmed that OTX2 was indeed expressed in G3/4-MB samples (Figure S4C). E33 and E12 were connected most closely with the others (Figure 2I), of which E33 demonstrated a significantly stronger correlation with *Otx2* expression (Table S4B).

Otx2 activation inhibits differentiation and keeps G3-MB in a progenitor-like state.[18] High *Otx2* expression correlated with an undifferentiated state, as well as enhanced cell division and invasion (Figure S4D). Based on these findings, we hypothesized that epigenetic regulation of *Otx2* enhancer (E33) played a crucial role in prog.like tumor cells. By grouping tumor cells according to DNA methylation levels, we observed that the hypomethylated subset presented stronger enrichment scores for gene signatures associated with early cerebellum development, cell cycle, and invasion (Figures 2J and S4E). Similarly, subsets with high CA of E33 showed robust cell division and invasion (Figure S4F). In contrast, low *Otx2* CA and expression subsets generally exhibited late UBC-like characteristics, indicating a more differentiated state (Figure S4F). Markers linking to metastasis (i.e., *Myc* and *Mmp2*) and proliferation (i.e., *Pcna* and *Mki67*) were widely expressed in hypomethylated subset (Figure S4G). These findings thus suggested that hypomethylation and high CA of E33 contributed to maintaining stemness.

To explore the relationship between E33 methylation and MB prognosis, we next analyzed MB clinicopathological characteristics to investigate the dependence of prognosis on epigenetic regulation. We stratified G3-MB patients based on the top 20% of low and high E33 methylation levels, finding that patients with lower methylation levels generally suffered from worse prognoses (Figure 2K). Both G3-MB and G4-MB subgroups were included in survival analysis, yielding similar results (Figure 2L; Table S4C). Multivariate analysis incorporating subgroup, gender, age, and metastasis status further supported that E33 could serve as an independent prognostic indicator in G3/4-MB patients (Figure 2M; Table S4D). Therefore, these data highly suggested that *Otx2* expression required SE hypomethylation, conferring a poor prognosis.

OTX2 feedforward autoregulation promoted G3-MB progression

As some TFs exhibit feedforward autoregulation,[18,19] we then examined whether OTX2 interacted with its SE. Chromatin immunoprecipitation sequencing (ChIP-seq) analysis of G3-MB cell line revealed the enriched H3K27ac signals and OTX2 binding at E33, indicating potential autoregulation[18] (Figure 3A). Given that enhancer-promoter proximity functions via chromatin loop structures,[37] we subsequently analyzed Hi-C (high-throughput chromosome conformation capture) chromosome conformation to confirm that E33 was spatially proximal to *Otx2* promoter[38] (Figure S5A). To recapitulate this potential autoactivation loop, we cloned the E33 containing an 8-bp consensus sequence (CGGATTAG), downstream of the *Otx2* promoter-driven reporter gene (Figure 3B). The E33-WT enhancer fragment can engage in spatial chromatin looping with the *Otx2* promoter, facilitating the co-recruitment of TFs,

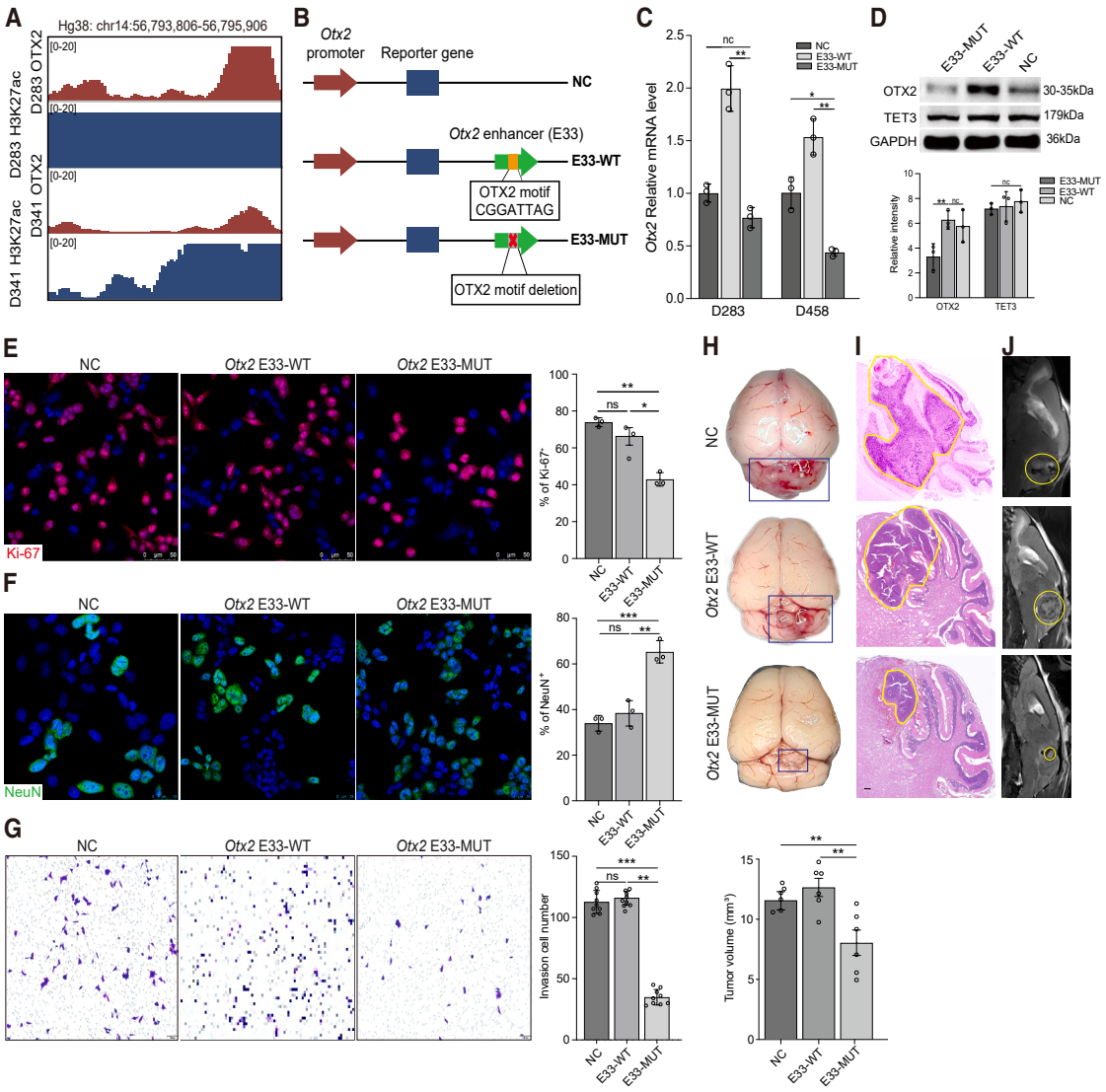

Figure 3. OTX2 feedforward autoregulation promotes G3-MB progression

(A) ChIP-seq analysis of the OTX2-binding sites associated with enhancer signature H3K27ac in D283 and D341 cells (GEO: GSE92585).

(B) Schematic model showing the reporter constructs of *Otx2* enhancer mutant. NC, non-coding; E33-WT, super-enhancer wild-type; E33-MUT, super-enhancer mutation.

(C) RT-qPCR analysis of *Otx2* mRNA levels in D283 and D458 cells transfected with *Otx2*-E33-MUT, WT, or NC plasmid. The relative mRNA level was calculated via $^{2-\Delta\Delta}$Ct method with 18-S RNA as an internal control, and the results are presented as fold changes against average values of E33-WT group. Data are presented as mean ± SEM. *$p < 0.05$ and **$p < 0.01$; two-tailed unpaired Student's *t* test.

(D) Immunoblotting analysis of OTX2 and TET3 expression in D283 cells transfected with *Otx2*-E33-MUT, WT, or NC plasmid.

(E) Representative images of Ki-67 expression in D283 cells transfected with *Otx2*-E33-MUT, WT, or NC plasmid ($n = 3$). Scale bar, 50 μm. Data are presented as mean ± SEM. *$p < 0.05$ and **$p < 0.01$; two-tailed unpaired Student's *t* test.

(F) Representative images of NeuN expression in D283 cells transfected with *Otx2*-E33-MUT, WT, or NC plasmids ($n = 3$). Scale bar, 50 μm. Data are presented as mean ± SEM. *$p < 0.05$, **$p < 0.01$, and ***$p < 0.001$; two-tailed unpaired Student's *t* test.

(G) Representative images showing the migration of D283 cells transfected with *Otx2*-E33-MUT, WT, and NC plasmids in the lower wells of Transwell system ($n = 3$). Scale bar, 100 μm. Data are presented as mean ± SEM. *$p < 0.05$, **$p < 0.01$, and ***$p < 0.001$; two-tailed unpaired Student's *t* test.

(H) Anatomic diagram showing the tumor volumes of intracranial xenografts derived from D283 cells infected with *Otx2*-E33-MUT, WT, or NC lentivirus.

(I) H&E staining showing the tumor volumes and cell morphology of xenografts in Figure 3H. Scale bar, 10 μm.

(J) Representative microMRI images showing the intracranial xenografts as shown in Figure 3H. Histogram showing the tumor volumes of cerebellar xenografts ($n = 6$).

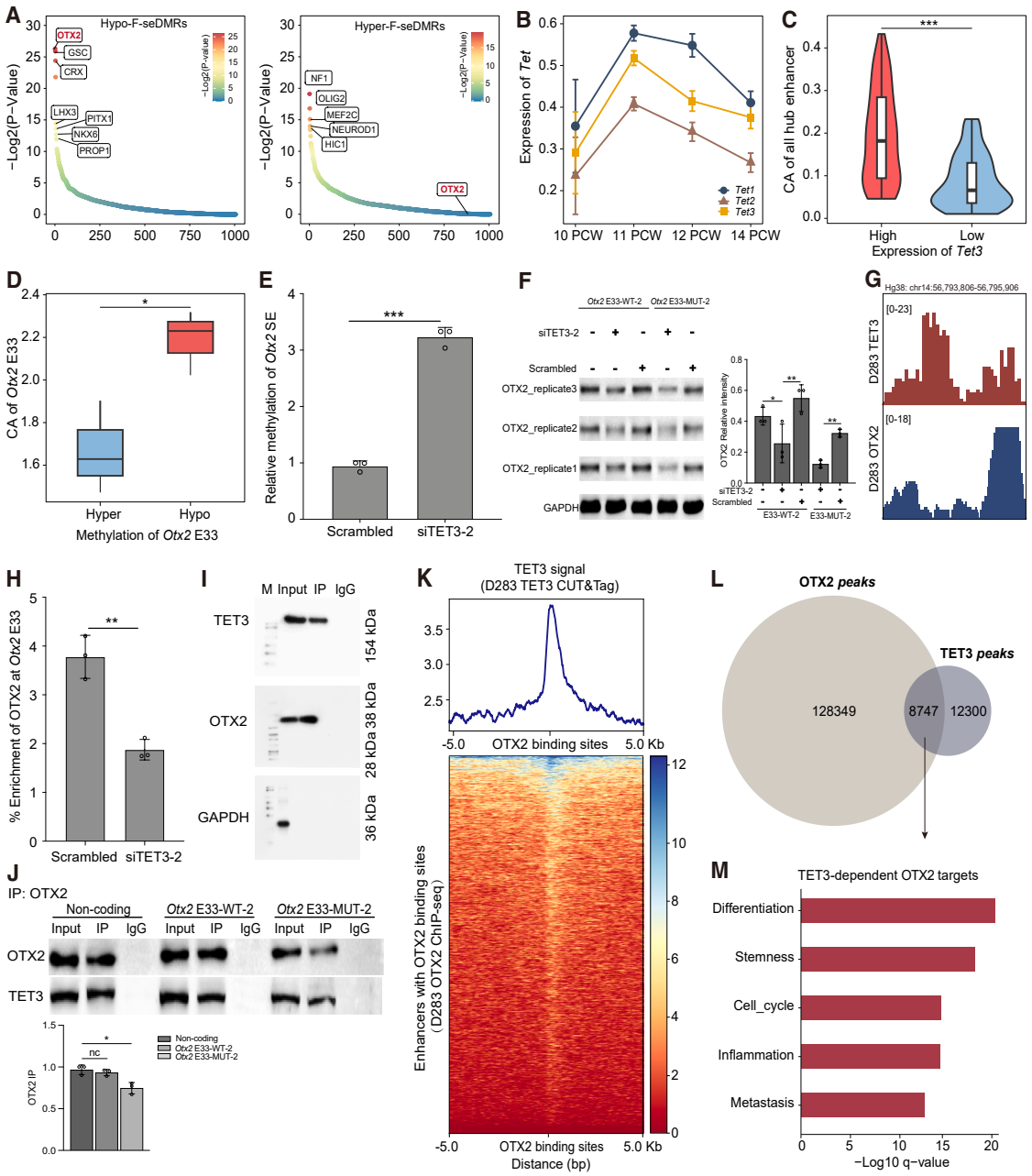

Figure 4. TET3 was recruited by OTX2 to demethylate the Otx2 SEs

(A) Scatterplots showing the enrichment of OTX2 binding sites in hypomethylated (left) and hypermethylated (right) regions. The scaled color bar represents the −Log2 (*p* value).

(B) Expression of ten-eleven translocation (TET) family members during cerebellum development from PCW10 to PCW14.

(C) Violin plot showing the CA levels of all hub SEs in the *Tet3* high- or low-expression subsets of G3-MB. *$p < 0.05$, **$p < 0.01$, and ***$p < 0.001$; two-tailed Mann-Whitney U test.

(D) Boxplot showing the CA levels of E33 (hub enhancer) in the *Otx2* hypomethylated and hypermethylated F-seDMR subsets of G3-MB. *$p < 0.05$, **$p < 0.01$, and ***$p < 0.001$; two-tailed Mann-Whitney U test.

(E) Quantitative methylation-specific PCR (qMSP) assay showing the relative DNA methylation levels of *Otx2* SE in D283 cells infected with scrambled siRNA or siTET3 ($n = 3$). Data are presented as mean ± SEM. *$p < 0.05$, **$p < 0.01$, and ***$p < 0.001$; two-tailed unpaired Student's *t* test.

(F) Western blot analysis showing the expression of OTX2 in D283 cells infected with scrambled siRNA or siTET3 following transfection of *Otx2* SE-WT and SE-MUT plasmids ($n = 3$). Data are presented as mean ± SEM. *$p < 0.05$ and **$p < 0.01$; two-tailed unpaired Student's *t* test.

(G) Genome track plot showing the overlap of TET3 cut-tag and OTX2 ChIP-seq signals within the OTX2 super-enhancer region in D283 cells.

(legend continued on next page)

the Mediator complex, chromatin remodeling complexes, and RNA polymerase II, thereby augmenting endogenous *Otx2* transcription and protein synthesis. In contrast, mutation of the binding site in E33-MUT abrogates interaction with the OTX2 TF, preventing formation of a functional activator complex and impairing recruitment of essential co-activators. This may also sequester other TFs in non-productive complexes, ultimately reducing *Otx2* mRNA and protein levels. We expressed these constructs in D283 and D458 cells. *Otx2* enhancer generated significantly higher transcriptional activity compared to the *Otx2* promoter alone. Deletion of OTX2 motif at E33 significantly decreased the O*tx2* transcriptional activity (Figures 3C and 3D). Collectively, OTX2, as a *trans*-acting factor, formed a positive feedback loop to autoregulate its own expression.

To gain deeper insight into the functions of E33, we conducted cell growth and invasion assays in MB cells transfected with plasmids targeting OTX2 motif at E33. This deletion mutation caused significantly abrogated proliferation and enhanced differentiation, as indicated by the decreased percentage of Ki-67$^+$ cells and increased proportion of NeuN$^+$ cells (Figures 3E and 3F). Similarly, aggressiveness was diminished in the OTX2 motif deletion condition (Figure 3G). To better corroborate the *in vitro* findings, we subcutaneously transplanted D283 cells infected with *Otx2* E33 mutation lentivirus and the control. Growth of xenografts was significantly compromised after the motif deletion mutation (Figures S5B and S5C). Proliferation was impaired, whereas dividing cells were predominant in control tissues (Figure S5D). Moreover, we generated cohorts of mice bearing E33 motif mutant or a wild-type D283 cell-derived orthotopic xenograft model. *Otx2* E33-deficient cells gave rise to much smaller masses, leading to a longer survival (Figures 3H–3J and S5E). Notably, the decreased percentage of Ki-67$^+$ and Sox2$^+$ cells and increased ratio of NeuN$^+$ cells indicated the remarkable inhibition of proliferation and stemness, accompanied by improved maturation (Figures S5F and S5G). Thus, these findings highlighted the dependency of tumor growth on the positive feedback autoregulation of *Otx2* E33.

OTX2-recruited TET3 demethylated the *Otx2* SEs

Since hypomethylation was associated with OTX2 binding at E33, we hypothesized that hypomethylation and OTX2 binding frequently colocalized. TFs enrichment analysis showed the OTX2 enrichment in hypomethylated SEs regions (Figure 4A). ChIP-seq profiles consistently showed the colocalization of OTX2-binding peaks with hypo-F-seDMRs in D341 and D283 cells,[19] implying a potential relationship between DNA hypomethylation and OTX2-binding activity (Figure S6A). Furthermore, comparison with normal cerebellum confirmed the restricted DNA methylation levels at OTX2-binding motif center (Figure S6B), in line with previous observations that OTX2-binding sites were prevalently located in DNA methylation valleys in MB.[24] These data suggested that OTX2 likely bound to the targeted hypomethylation sites.

Hypomethylation of enhancers may result from the activation of demethylases and the deactivation of methyltransferases. Therefore, we evaluated the expression levels of the DNMT and TET families in tumor tissues (Figures 4B, S6C, and S6D). All members of both families were upregulated in G3-MB and peaked at 11 post-conception weeks (PCWs) during cerebellum development, coinciding with formation of RL^{SVZ}, and then gradually declined[5,38,39] (Figures 4B, S6C, and S6D). This pattern suggested that TET, not DNMT, contributed to hypomethylation. TET3, in particular, is crucial for *Otx2* expression, as shown in *Tet3* knockout embryonic stem cells.[40,41] Disruption of *Tet3* and *Otx2* probably led to the development failure and tumor initiation. *Tet3* expression positively correlated with *Otx2* expression in our and an independent MB cohort[2] (Figure S6E). However, OTX2-KD snRNA-seq analysis revealed that *Tet3* expression was not affected by silencing *Otx2*[5] (Figure S6F), speculating that TET3 might mediate *Otx2* expression. The spatiotemporal transcriptome atlas of developing human brain showed that *Tet3* expression was increased in RL, the origin of G3-MB, from 10 PCW to 14 PCW[29,42] (Figure S6G), indicative of a potential role of *Tet3* in tumorigenesis. Moreover, *Tet3* expression was higher in G3-MB_alpha compared to other subtypes (Figures S6H and S6I), aligning with elevated *Otx2* levels (Figures S6J and S6K). It was speculated that TET3-induced demethylation enhanced *Otx2* transcription. To test this hypothesis, we stratified G3-MB cases and found that the high-*Tet3*-expressing subset corresponded to boosted CA (Figure 4C). In detail, abundantly accessible chromatin was observed at *Otx2* hypomethylated E33, the currently designed deletion mutation segment (Figure 4D). To better confirm the effects of TET3 on *Otx2* expression, we constructed short-interfering RNAs (siRNAs) to deplete *Tet3* (Figure S7A). In *Tet3*-low D283 cells, increased *Otx2* SEs methylation indicated that hypomethylation depended on TET3. *Otx2* expression was decreased demonstrating that TET3-mediated SE hypomethylation promoted *Otx2* expression (Figures 4E, 4F, and S7B). *Otx2*-overexpressing and empty vector control D283 MB cells were treated with the TET3 inhibitor Bobcat339. Proliferation assays showed that exogenous *Otx2* upregulation promoted tumor cell proliferation despite TET3 inhibition (Figure S7C). These findings indicate that *Otx2* overexpression can override the proliferative suppression caused by TET3 inhibition, suggesting that *Otx2* functions downstream of TET3 to drive tumor cell growth.

(H) Chromatin immunoprecipitation (ChIP)-qPCR analysis of OTX2 at the *Otx2* SE in D283 cells infected with scrambled siRNA or siTET3 (Figure S7F). Data are presented as mean ± SEM. *$p < 0.05$ and **$p < 0.01$; two-tailed unpaired Student's *t* test.

(I) Endogenous co-immunoprecipitation (coIP) assay with OTX2 and TET3 in D283 cells and immunoblotting analysis examining the expression of OTX2 and TET3.

(J) Immunoprecipitation assay with OTX2 in D283 cells transfected with non-coding, *Otx2* SE-WT, and SE-MUT plasmids. Data are presented as mean ± SEM. *$p < 0.05$; two-tailed unpaired Student's *t* test.

(K) Average density plot and heatmap of TET3 signals at *Otx2* hypomethylated SE in D283 cells.

(L) Venn diagram showing the overlap between OTX2-binding peaks and TET3-binding peaks in D283 cells.

(M) Barplot showing the enrichment pathways of TET3-dependent *Otx2* F-seDMR-targeted genes.

To detect the TET3-binding sites, cleavage under target and tagmentation sequencing (CUT&Tag-seq) was performed on D283 cells using the anti-TET3 antibody (Table S5). Integration with D283 OTX2 ChIP-seq data revealed the colocalization of TET3 and OTX2 at binding sites within *Otx2* SE[19] (Figure 4G). ChIP-qPCR using an anti-OTX2 antibody demonstrated that *Tet3* silencing significantly reduced OTX2's binding to *Otx2* E33 (Figures 4H and S7F). Immunostaining in G3-MB cells showed colocalization of OTX2 and TET3 (Figure S7G). However, the fact that TET3 lacks DNA-binding specificity in genome prompted us to explore whether OTX2 preferentially recruited this methyl eraser to *Otx2* SEs. Accordingly, co-immunoprecipitation confirmed the physical interaction between endogenous OTX2 and TET3, and E33 mutation significantly weakened this association. (Figures 4I and 4J). Actually, about half of TET3-binding sites overlapped with a large number of OTX2-binding sites, particularly in SEs (Figures 4K, 4L, and S7D). DNA methylation near these overlapping sites presented significantly reduced (Figure S7E). TET3-dependent OTX2-targeted genes were predominantly enriched in the process of stemness and differentiation reprogramming (Figure 4M), as confirmed by the expression of SOX2, PBX3 (early GN marker), and EOMES (early UBC marker; Figure S7H). Viability was significantly reduced upon TET3 interference (Figure S7I), confirming the importance of demethylases in G3-MB. Overall, these data suggested that OTX2-recruited TET3 potentially instigated hypomethylation within *cis*-regulatory elements.

Downregulation of TET3 attenuated G3-MB progression *in vivo*

Then we detected whether targeting TET3 could suppress tumor progression. Given that inhibitors exert strong toxicity on the nervous system and that siRNAs are easily degraded *in vivo*, nanoparticles including LNPs, poly lactic-co-glycolic acid, and zeolitic imidazolate framework-8 (ZIF8) were designed for intraventricular delivery (Figures 5A and S8A). Firstly, LNPs were used to coat the reagent or siTET3 (Figure 5A). Bobcat339 has been previously reported to bind to catalytic pockets of TET2/3,[43,44] also verified in the current study (Figure S8B).[45] Homogeneous spherical LNPs with a size of nearly 100 nm were constructed (Figures 5B and 5C), harboring negative zeta potentials of −10.8 mV for LNP@Bobcat339 and −12.2 mV for LNP@siTET3 (Figure 5D). We tracked LNP-loaded siRNAs in the murine brain and xenografts using Cy5 fluorescence. The Cy5 label was inserted into the siRNA sequence. After intracerebroventricular injection, the signal was mainly in the tumor region (Figure 5E). At 5–6 h after injection, most siRNAs were degraded, and only minimal fluorescence was seen in the central nervous system (Figure 5E). When phalloidin-labeled cytoskeleton was colocalized, LNP@siTET3 was observed in a majority of cells (Figure 5F), demonstrating efficient delivery. The fact that vital organs were not damaged indicated no significant toxicity (Figure S8C). Animals injected intraventricularly with uncoated Bobcat339 presented a significant decrease in body weight (Figure S8D), implying that nanoparticle encapsulation decreased toxicity.

Human G3-MB tumor tissues were collected intraoperatively and subsequently bioprinted into a hydrogel matrix using bioink.[46] Cell viability assays revealed a marked reduction in proliferative capacity in the LNP@siTET3-treated group compared to controls (Figure 5G). To avoid damage associated with repeated punctures and anesthesia, we implemented the catheterization in immunodeficient rats for multiple intraventricular medications without anesthesia (Figure 5A and Video S1). Four days following the transplantation of cerebellar allograft G3-MB models, we treated the animals through catheterization with LNP@Bobcat339 or vehicle control once every day. Growth of xenografts after TET3 interference was significantly reduced, as indicated by a survival benefit (Figure S8E). In the experimental group, amounts of impaired dividing cells and increased differentiated cells were observed (Figures 5H–5J). The discounted MMP9 expression indicated weakened tumor invasiveness (Figure 5J). Similarly, mice bearing cerebellar PDXs (patient-derived xenografts) received intraventricular administration of LNP@siTET3 or the control once every day. MicroMRI revealed that LNP@siTET3 powerfully inhibited tumor growth at more than 50% dilution, and the animals benefited from longer survivals (Figure 5K and S8F–S8G). Histologically, proliferating tumor cells massively accumulated in controls. However, few Ki-67$^+$ cells were observed across tumor tissues following LNP@siTET3 treatment, and a majority were under differentiation, as verified by another PDX line (Figures S8H and S8I). As predicted, OTX2 expression in LNP@siTET3-generated xenografts dramatically declined, further confirming that ablation of TET3 significantly prohibited *Otx2* activation (Figure S8J). The other two nanoparticle deliveries did not demonstrate significant antitumor efficacy (data not shown). Taken together, these findings indicated that targeting the TET3-*Otx2* SE axis represented a promising approach to combat G3-MB progression.

TGF-β1/Smad2 signaling activated the TET3

A previous study identified a TET3/transforming growth factor β1 (TGF-β1)-positive feedback loop in liver fibrosis.[47] To assess whether TET3 activation was mediated by TGF-β1 via Smads, RNA-seq analysis reflected the common activation of TGF-β1/Smads axis in G3-MB[2] (Figure S9A), with this signaling positively correlating with *Tet3* expression (Figure S9B). An approximately 2-fold reduction in DNA methylation was detected in TGF-β1/Smads-activated background, albeit with a similar variation to above results (Figure S9C). Subsequent exploration linking TET3 activation with Smads complex motif displayed a positive correlation and broadly bound sites on *Tet3* promoter (Figures S9D and S9E).

To better corroborate our bioinformatic findings, D283 cells were cultured in the presence of exogenous TGF-β1 at two candidate concentrations and then evaluated for downstream cascades. Treatment of D283 cells with TGF-β1 significantly increased *Tet3* mRNA levels ($p < 0.01$; Figure S9F), indicating transcriptional activation by TGF-β1. Consistent with this, immunoblot analysis demonstrated that TGF-β1 stimulation markedly upregulated TET3 protein expression compared to untreated controls (Figure S9G, lanes 1 vs. 2). To determine the functional role of TET3 in TGF-β1-mediated OTX2 induction, we performed siRNA-mediated knockdown of TET3 (siTET3) in TGF-β1-stimulated cells. This intervention significantly reduced both TET3 and OTX2 protein levels (Figure S9G, lanes 3 vs. 4). In contrast,

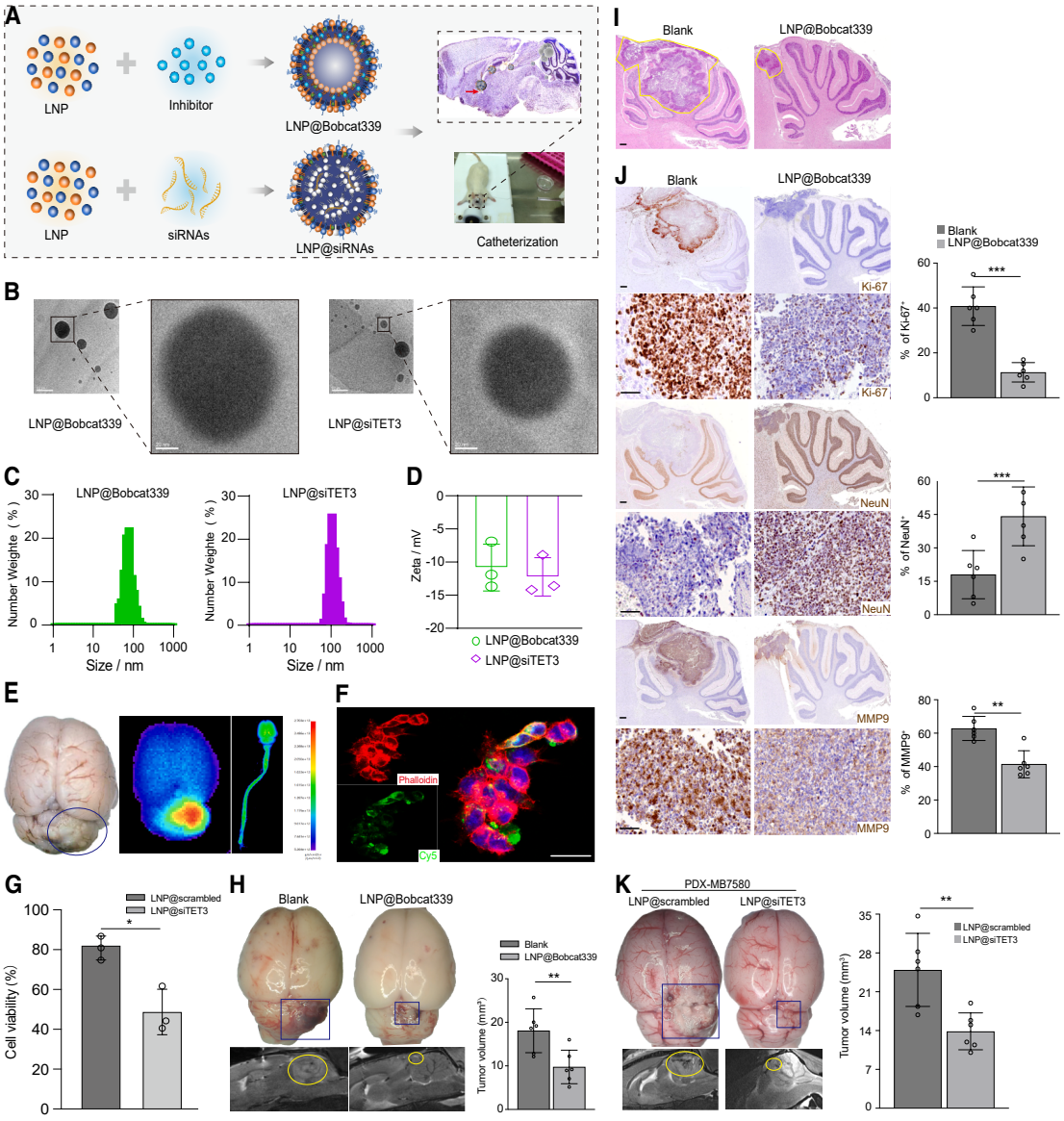

Figure 5. Nanoparticle-loaded inhibitor or siTET3 suppressed G3-MB progression

(A) Schematic model displaying the assembly process of LNP and TET3 inhibitors or siRNAs to treat the cerebellar xenografts via intraventricular administration.

(B) Transmission electron microscope (TEM) investigations exhibiting the spherical morphology of LNP@Bobcat339 and LNP@siTET3. Scale bar, 20 nm.

(C) Peak charts showing the weight and size of LNP@Bobcat339 and LNP@siTET3.

(D) Barplot showing the Zeta potentials of LNP@Bobcat339 and LNP@siTET3.

(E) Small animal *in vivo* fluorescence image showing the enrichment of LNP@siTET3 in xenografts derived from human G3-MB. Cy5 labeling of the nanoparticle-coated siRNAs.

(F) Immunofluorescence staining showing the location of LNP@siTET3 in D283 cells. Cy5 labeling of the nanoparticle-coated siRNAs. Scale bar, 10 μm.

(G) Cell viability analysis showing the proliferation of primary human G3-MB 3D bioprint organoids. Data are presented as mean ± SEM. $^{*}p < 0.05$; two-tailed unpaired Student's *t* test.

(H) Representative anatomic diagram and microMRI images showing intracranial xenografts (PDX-MB7580) following intraventricular treatment of LNP@Bobcat339 and blank LNPs ($n = 6$). $^{**}p < 0.01$.

(I) Representative H&E staining showing the tumor volume of two subgroups (Figure 5H). Scale bar, 10 μm.

(J) Immunostaining for Ki-67, NeuN, and MMP9 expression in tumor tissues as shown in Figure 5H. Scale bar, 10 μm. Data are presented as mean ± SEM. $^{*}p < 0.05$, $^{**}p < 0.01$, and $^{***}p < 0.001$; two-tailed unpaired Student's *t* test.

(K) Representative images and microMRI images showing the intracranial xenografts (PDX-MB7580) following the intraventricular treatment with LNP@siTET3 or LNP@scrambled ($n = 6$). Data are presented as mean ± SEM. $^{*}p < 0.05$ and $^{**}p < 0.01$; two-tailed unpaired Student's *t* test.

scrambled siRNA controls maintained robust TGF-β1-induced TET3 and OTX2 expression (Figure S9G, lane 4). Collectively, these results establish TET3 as a TGF-β1-induced effector essential for OTX2 upregulation. Tumor proliferation and stemness were implied by elevated levels of TGF-β1/Smads in prog. like and cycling cells (Figures S9H and S9I). To functionally validate this association, we exposed D283 cells (representing a progenitor-like model) to TGF-β1 for 72 h. This treatment significantly enhanced proliferation and invasion (Figures S9J–S9L), confirming the pro-tumorigenic role of TGF-β1. Critically, TET3 knockdown suppressed TGF-β1-induced proliferation and invasion (Figures S9J–S9L). In summary, we propose a model that OTX2-recruited TET3 demethylated *Otx2* SEs to activate its self-reinforcing transcription program, triggered by TGF-β1/Smads signaling, which may emerge as a key target for G3-MB (Figure S9M).

DISCUSSION

The strong stemness of G3-MB, leading to treatment resistance, remains a challenging issue for clinicians. Herein, we identified *Otx2* hypo-F-seDMRs had significant prognostic implications for G3-MB patients. Furthermore, as a TF, OTX2 guiding TET3, autoregulated genome-wide demethylation at specific SEs to promote G3-MB progression. Then, LNP-loaded siTET3 or Bobcat339 significantly suppressed cerebellar allograft growth.

A previous study elucidated the influence of DNA methylation on SE function.[48] However, owing to limited resolution profiling of MB, understanding of DNA methylation patterns and regulatory mechanisms at gene-distal *cis*-regulatory regions remains limited. In this study, we comprehensively examined SE DNA methylation in MB via WGBS. One *Otx2* "hub enhancer" domain, E33, was of paramount importance, exhibiting a negative correlation between DNA methylation and CA. Many methylated sites within this region were not covered by DNA methylation arrays but were observed in a whole-genome bisulfite-based study.[49] WGBS outperforms methylation arrays by providing a thorough view of DNA methylation patterns across the entire genome, unearthing both known and novel sites.[50–53] Its ultrahigh resolution enables in-depth exploration of biological mechanisms in various conditions, such as prostate cancer, glioblastoma, azoospermia, and cardiovascular disease.[24,54]

Another key discovery is the involvement of TET3 in site-specific hypomethylation within G3-MB F-seDMRs. Among broad demethylated binding motifs, TET3 was located specifically in F-seDMRs, self-guided by OTX2. Previously, Boulay G. reported that *Otx2* activity at SEs influenced targeted gene expression,[19] complemented by current evidence linking it to TET3-mediated hypomethylation of F-seDMRs. The physical interaction between OTX2 and TET3 at the single-molecule level endowed TET3 with specificity toward OTX2 motifs, thereby enabling targeted demethylation. Our study unveiled how TET3-mediated hypomethylation sustained the activity of OTX2-centered SE network during tumorigenesis, shedding light on upstream regulatory mechanisms of gene activation.

Beyond its established OTX2-directed role, TET3 displays additional multifunctionality in cell-cycle control and DNA damage response.[55] Consistent with these functions, TET3 is markedly upregulated in cisplatin-resistant ovarian cancer cells.[56] In glioblastoma, STAT3-recruited TET3 catalyzes promoter hydroxymethylation at genes governing stemness, survival, and proliferation, thereby promoting tumorigenicity and chemoresistance.[57] Intriguingly, our preliminary explorations in G3-MB suggest that TET3 may also associate with hypomethylated loci distinct from OTX2 targets, potentially linked to cell-cycle progression, hypoxia adaptation, and tumor cell quiescence programs. Although systematic validation is necessary, this potential functional expansion implies that TET3 could collectively enhance cellular fitness within therapy-resistant MB microenvironments.

TET family catalyzes DNA demethylation by converting 5mC (5-methylcytosine) to 5hmC (5-hydroxymethylcytosine),[58] crucial for neuroectodermal and mesodermal fate determination.[59] TET3 exhibited robust activity in the embryonic cerebellum during RL^{SVZ} formation at PCW11. TET3 plays a pivotal role in the nervous system, efficiently converting fibroblasts into functional neurons.[60] Bobcat339, a small synthetic molecule modulating TET3 in AgRP (agouti-related peptide) neurons, alleviates anorexia nervosa.[44] Encapsulating reagents within nanoparticles via intraventricular delivery resulted in a 5- to 10-fold augmentation in cerebrospinal fluid concentration. Early studies showed that Bobcat339 primarily inhibited TET2.[61] Our experiments, consistent with Lv H's finding, supported its ability to block TET3. Nanoparticle delivery circumvents rapid siRNA degradation upon *in vivo* administration,[62] suggesting a novel therapeutic approach. Future peripheral blood transfusion of nanoparticle-loaded siRNAs may minimize hepatic and splenic accumulation while traversing blood-brain barrier.

TGF-β1 signaling controls a wide range of biological processes, spanning from embryonic development to cancer progression.[63] A comprehensive genomic analysis of G3-MB uncovered recurrent focal CNVs affecting genes within TGF-β signaling cascades.[3] Additionally, aberrant SE instigation in G3-MB, as revealed by H3K27ac ChIP-seq profiling,[25] indicated increased TGF-β1 signaling activity. TGF-β1/PTEN signaling also modulates G3-MB metastasis.[64] We have identified Smad complex binding sites on the *Tet3* promoter, illustrating how TGF-β1 signaling upregulated TET3, thereby facilitating downstream demethylation. The dual role of TGF-β1 signaling as both a tumor suppressor and promoter poses challenges for cancer therapy. In forthcoming research, we aim to engineer TGF-β1 as the warhead of LNP, precisely targeting overexpressed receptors to deliver encapsulated reagents or siRNAs with high specificity.[65]

Limitations of the study

While our study demonstrates the prognostic significance of *Otx2* hypo-F-seDMRs in G3-MB and establishes a therapeutic strategy targeting the *Otx2*-TET3 axis, several limitations should be acknowledged. First, although WGBS provides high-resolution methylation profiles, the cohort size of G3-MB patients analyzed may limit the statistical power to generalize the prognostic correlations across diverse clinical subgroups. Second, although Bobcat339 showed efficacy in blocking TET3, its potential off-target effects on other TET family members (e.g.,

CellPress
OPEN ACCESS

TET2) and long-term safety profiles in the central nervous system require further characterization. Finally, while nanoparticle delivery enhanced cerebrospinal fluid bioavailability, the translational feasibility of this approach, including blood-brain barrier penetration efficiency and immune compatibility, needs systematic evaluation.

RESOURCE AVAILABILITY

Lead contact

Requests for further information and resources and reagents will be fulfilled by the lead contact, Hailong Liu (liuhailonger@163.com).

Materials availability

Otx2 SE mutant plasmids and *Otx2* SE wild-type plasmids generated in this study are available from the lead contact upon request for tumor- or disease-related research. Applicants must specify the intended purpose and main application in their request.

Data and code availability

The WGBS dataset is deposited in the CNGB database (CNGB: CNP0005827). The single-nucleus RNA and ATAC-seq data are deposited in the CNGB database (CNGB: CNP0006024). The bulk RNA-seq data are deposited in the CNGB database (CNGB: CNP0006024). The CUT&Tag-seq data are deposited in the CNGB database (CNGB: CNP0006023). The ChIP-seq data are available in the GEO database (GEO: GSE92585), and Hi-C data are available in the GEO database (GEO: GSE198565). The published DNA methylation array and RNA-seq data of MB are available in the GEO database (GEO: GSE85217). The published WGBS data of cerebellum are deposited in the EGA database (EGA: EGAS00001000561). This study does not report any custom code. Any additional information required to reanalyze the data reported in this paper is available from the lead contact upon request.

ACKNOWLEDGMENTS

We thank Dr. Zhong Ma (Sanbo Brain Hospital Capital Medical University) for interpretation of pathological data. The current study was supported by the Tian Qi High Performance Computing Center and the Biomedical High Performance Computing Platform. We are especially grateful to China National Clinical Research Center for Neurological Diseases and Chinese Academy of Medical Sciences for their assistance.

This work was supported by the Natural Science Foundation of Beijing (L232079), National Key Research and Development Program of China (2022ZD0210100), National Natural Science Foundation of China (82273343, 82172608, 82101356, and 81902975), National Science Fund of Beijing for Distinguished Young Scholars (JQ24040), Beijing Nova Star Program (20220484058), and Capital Medical University Fund for Excellent Young Scholars (KCB2304).

AUTHOR CONTRIBUTIONS

Designing research studies, H.L., T.J., M.D.T., and G.L.L.; conducting experiments, H.L., T.J., X.C., Y. Song., J.Z., L.D.H., A.R., X.W., E.Y.W., Y. Su., F.L., H.Y., Z.Z., Z.W., and Y. Sun; data collection, X.C., H.L., X. Qiu, C.L., T.J., D.H., Y.L., K.D., D.W., and Z.F.; bioinformatics analysis, X.C., Z.W., M.L., and Z.L.; functional experiments, F.L., H.L., W.W., Y.W., and Y.-q.L.; software, O.S., T.Y., Y. Shi, and Y.J.; providing reagents, Y. Song. and G.L.L.; survival analysis, Y. Su. and Y.T.; data interpretation, H.L., X.C., Y.T., X. Qi, S.L., and Y. Song.; writing and editing, H.L., M.D.T., C.D., X.C., Y.Z., and Y. Su.; funding acquisition, H.L. and T.J.; supervision, M.D.T., H.L., T.J., and G.L.L. All authors read and approved the final version of the manuscript. The method used in the current study assigned the authorship order among the co-first authors.

DECLARATION OF INTERESTS

The authors declare no competing interests.

STAR★METHODS

Detailed methods are provided in the online version of this paper and include the following:

- KEY RESOURCES TABLE
- EXPERIMENTAL MODEL AND SUBJECT DETAILS
  - Patients and samples
  - Cells
  - Experimental animal sourcing and housing
  - Mouse models of G3-MB
- METHOD DETAILS
  - WGBS data processing
  - Bulk gene expression profiling
  - Unsupervised molecular subgroup analysis
  - G3-MB subtype identification
  - DMRs analysis and annotation
  - Identification of functional differentially methylated regions (F-DMRs)
  - CNV analysis
  - Gene set enrichment analysis
  - *Otx2* SEs methylation-dependent differentiation potential
  - Construction of single-gene enhancer networks
  - *Otx2* enhancer interaction network analysis
  - snRNA-seq suspension preparation
  - snRNA-seq library preparation
  - snRNA-seq data processing
  - Ambient RNA mitigation
  - Doublet exclusion
  - snATAC-seq data processing
  - Cell clustering and cell-type identification in snRNA-seq dataset
  - Integration of snRNA-seq and snATAC-seq data
  - Identification of DEGs and GO enrichment
  - Transcription factor motif enrichment analysis
  - Scoring of the TGF-β-Smad signaling pathway
  - Gene Expression Omnibus and European Genome-phenome archive data validation
  - CUT&Tag-seq
  - Visualization of ChIP-seq, Hi-C data and CUT&Tag-seq
  - Reagents
  - Nanoparticle-loaded Bobcat339 or siRNA construction
  - H.&E., immunohistochemistry and immunofluorescence staining
  - CCK8 examination
  - Transwell assay
  - Plasmid transfection
  - RNA extraction and qRT−PCR
  - Cell lysis
  - Immunoblotting analysis
  - Co-immunoprecipitation (Co-IP)
  - ChIP−qRT−PCR
  - Quantitative methylation-specific PCR (qMSP)
  - Three-dimensional (3D) bioprinted MB tetra-culture models
  - Treatments in rats
- QUANTIFICATION AND STATISTICAL ANALYSIS

SUPPLEMENTAL INFORMATION

Supplemental information can be found online at https://doi.org/10.1016/j.xcrm.2025.102474.

Received: March 7, 2025
Revised: August 21, 2025
Accepted: November 4, 2025
Published: December 2, 2025

REFERENCES

1. Northcott, P.A., Korshunov, A., Pfister, S.M., and Taylor, M.D. (2012). The clinical implications of medulloblastoma subgroups. Nat. Rev. Neurol. *8*, 340–351.
2. Cavalli, F.M.G., Remke, M., Rampasek, L., Peacock, J., Shih, D.J.H., Luu, B., Garzia, L., Torchia, J., Nor, C., Morrissy, A.S., et al. (2017). Intertumoral Heterogeneity within Medulloblastoma Subgroups. Cancer Cell *31*, 737–754.e6.
3. Northcott, P.A., Shih, D.J.H., Peacock, J., Garzia, L., Morrissy, A.S., Zichner, T., Stütz, A.M., Korshunov, A., Reimand, J., Schumacher, S.E., et al. (2012). Subgroup-specific structural variation across 1,000 medulloblastoma genomes. Nature *488*, 49–56.
4. Liu, H., Zhang, J., Wang, Z., Wang, W., Han, D., Chen, X., Su, Y., Zhang, J., Daniels, C., Saulnier, O., et al. (2025). High cellular plasticity state of medulloblastoma local recurrence and distant dissemination. Cell Rep. Med. *6*, 101914.
5. Hendrikse, L.D., Haldipur, P., Saulnier, O., Millman, J., Sjoboen, A.H., Erickson, A.W., Ong, W., Gordon, V., Coudière-Morrison, L., Mercier, A.L., et al. (2022). Failure of human rhombic lip differentiation underlies medulloblastoma formation. Nature *609*, 1021–1028.
6. Lytle, N.K., Barber, A.G., and Reya, T. (2018). Stem cell fate in cancer growth, progression and therapy resistance. Nat. Rev. Cancer *18*, 669–680.
7. Ye, Z.N., Yu, M.Y., Kong, L.M., Wang, W.H., Yang, Y.F., Liu, J.Q., Qiu, M.H., and Li, Y. (2015). Biflavone Ginkgetin, a Novel Wnt Inhibitor, Suppresses the Growth of Medulloblastoma. Nat. Prod. Bioprospect. *5*, 91–97.
8. Robinson, G.W., Orr, B.A., Wu, G., Gururangan, S., Lin, T., Qaddoumi, I., Packer, R.J., Goldman, S., Prados, M.D., Desjardins, A., et al. (2015). Vismodegib Exerts Targeted Efficacy Against Recurrent Sonic Hedgehog-Subgroup Medulloblastoma: Results From Phase II Pediatric Brain Tumor Consortium Studies PBTC-025B and PBTC-032. J. Clin. Oncol. *33*, 2646–2654.
9. Northcott, P.A., Jones, D.T.W., Kool, M., Robinson, G.W., Gilbertson, R.J., Cho, Y.J., Pomeroy, S.L., Korshunov, A., Lichter, P., Taylor, M.D., and Pfister, S.M. (2012). Medulloblastomics: the end of the beginning. Nat. Rev. Cancer *12*, 818–834.
10. Bandopadhayay, P., Piccioni, F., O'Rourke, R., Ho, P., Gonzalez, E.M., Buchan, G., Qian, K., Gionet, G., Girard, E., Coxon, M., et al. (2019). Neuronal differentiation and cell-cycle programs mediate response to BET-bromodomain inhibition in MYC-driven medulloblastoma. Nat. Commun. *10*, 2400.
11. Ecker, J., Oehme, I., Mazitschek, R., Korshunov, A., Kool, M., Hielscher, T., Kiss, J., Selt, F., Konrad, C., Lodrini, M., et al. (2015). Targeting class I histone deacetylase 2 in MYC amplified group 3 medulloblastoma. Acta Neuropathol. Commun. *3*, 22.
12. da Cunha Jaeger, M., Ghisleni, E.C., Cardoso, P.S., Siniglaglia, M., Falcon, T., Brunetto, A.T., Brunetto, A.L., de Farias, C.B., Taylor, M.D., Nör, C., et al. (2020). HDAC and MAPK/ERK Inhibitors Cooperate To Reduce Viability and Stemness in Medulloblastoma. J. Mol. Neurosci. *70*, 981–992.
13. Hnisz, D., Abraham, B.J., Lee, T.I., Lau, A., Saint-André, V., Sigova, A.A., Hoke, H.A., and Young, R.A. (2013). Super-enhancers in the control of cell identity and disease. Cell *155*, 934–947.
14. Northcott, P.A., Lee, C., Zichner, T., Stütz, A.M., Erkek, S., Kawauchi, D., Shih, D.J.H., Hovestadt, V., Zapatka, M., Sturm, D., et al. (2014). Enhancer hijacking activates GFI1 family oncogenes in medulloblastoma. Nature *511*, 428–434.
15. Robinson, G.W., Rudneva, V.A., Buchhalter, I., Billups, C.A., Waszak, S.M., Smith, K.S., Bowers, D.C., Bendel, A., Fisher, P.G., Partap, S., et al. (2018). Risk-adapted therapy for young children with medulloblastoma (SJYC07): therapeutic and molecular outcomes from a multicentre, phase 2 trial. Lancet Oncol. *19*, 768–784.
16. He, Y.F., Li, B.Z., Li, Z., Liu, P., Wang, Y., Tang, Q., Ding, J., Jia, Y., Chen, Z., Li, L., et al. (2011). Tet-mediated formation of 5-carboxylcytosine and its excision by TDG in mammalian DNA. Science *333*, 1303–1307.
17. Flam, E.L., Danilova, L., Kelley, D.Z., Stavrovskaya, E., Guo, T., Considine, M., Qian, J., Califano, J.A., Favorov, A., Fertig, E.J., and Gaykalova, D.A. (2019). Differentially Methylated Super-Enhancers Regulate Target Gene Expression in Human Cancer. Sci. Rep. *9*, 15034.
18. Stromecki, M., Tatari, N., Morrison, L.C., Kaur, R., Zagozewski, J., Palidwor, G., Ramaswamy, V., Skowron, P., Wölfl, M., Milde, T., et al. (2018). Characterization of a novel OTX2-driven stem cell program in Group 3 and Group 4 medulloblastoma. Mol. Oncol. *12*, 495–513.
19. Boulay, G., Awad, M.E., Riggi, N., Archer, T.C., Iyer, S., Boonseng, W.E., Rossetti, N.E., Naigles, B., Rengarajan, S., Volorio, A., et al. (2017). OTX2 Activity at Distal Regulatory Elements Shapes the Chromatin Landscape of Group 3 Medulloblastoma. Cancer Discov. *7*, 288–301.
20. Ziller, M.J., Hansen, K.D., Meissner, A., and Aryee, M.J. (2015). Coverage recommendations for methylation analysis by whole-genome bisulfite sequencing. Nat. Methods *12*, 230–232.
21. Zhang, L., Gu, C., Yang, L., Tang, F., and Gao, Y.Q. (2017). The sequence preference of DNA methylation variation in mammalians. PLoS One *12*, e0186559.
22. Hovestadt, V., Ayrault, O., Swartling, F.J., Robinson, G.W., Pfister, S.M., and Northcott, P.A. (2020). Medulloblastomics revisited: biological and clinical insights from thousands of patients. Nat. Rev. Cancer *20*, 42–56.
23. Jones, P.A. (2012). Functions of DNA methylation: islands, start sites, gene bodies and beyond. Nat. Rev. Genet. *13*, 484–492.
24. Hovestadt, V., Jones, D.T.W., Picelli, S., Wang, W., Kool, M., Northcott, P.A., Sultan, M., Stachurski, K., Ryzhova, M., Warnatz, H.J., et al. (2014). Decoding the regulatory landscape of medulloblastoma using DNA methylation sequencing. Nature *510*, 537–541.
25. Lin, C.Y., Erkek, S., Tong, Y., Yin, L., Federation, A.J., Zapatka, M., Haldipur, P., Kawauchi, D., Risch, T., Warnatz, H.J., et al. (2016). Active medulloblastoma enhancers reveal subgroup-specific cellular origins. Nature *530*, 57–62.
26. Sepp, M., Leiss, K., Murat, F., Okonechnikov, K., Joshi, P., Leushkin, E., Spänig, L., Mbengue, N., Schneider, C., Schmidt, J., and Trost, N. (2023). Cellular development and evolution of the mammalian cerebellum. Nature *625*, 788–796.
27. Vladoiu, M.C., El-Hamamy, I., Donovan, L.K., Farooq, H., Holgado, B.L., Sundaravadanam, Y., Ramaswamy, V., Hendrikse, L.D., Kumar, S., Mack, S.C., et al. (2019). Childhood cerebellar tumours mirror conserved fetal transcriptional programs. Nature *572*, 67–73.
28. Aldinger, K.A., Thomson, Z., Phelps, I.G., Haldipur, P., Deng, M., Timms, A.E., Hirano, M., Santpere, G., Roco, C., Rosenberg, A.B., et al. (2021). Spatial and cell type transcriptional landscape of human cerebellar development. Nat. Neurosci. *24*, 1163–1175.
29. Zhong, S., Wang, M., Huang, L., Chen, Y., Ge, Y., Zhang, J., Shi, Y., Dong, H., Zhou, X., Wang, B., et al. (2023). Single-cell epigenomics and spatiotemporal transcriptomics reveal human cerebellar development. Nat. Commun. *14*, 7613.
30. Chang, W., Zhao, Y., Rayêe, D., Xie, Q., Suzuki, M., Zheng, D., and Cvekl, A. (2023). Dynamic changes in whole genome DNA methylation, chromatin and gene expression during mouse lens differentiation. Epigenetics Chromatin *16*, 4.
31. Hovestadt, V., Smith, K.S., Bihannic, L., Filbin, M.G., Shaw, M.L., Baumgartner, A., DeWitt, J.C., Groves, A., Mayr, L., Weisman, H.R., et al. (2019). Resolving medulloblastoma cellular architecture by single-cell genomics. Nature *572*, 74–79.
32. Smith, K.S., Bihannic, L., Gudenas, B.L., Haldipur, P., Tao, R., Gao, Q., Li, Y., Aldinger, K.A., Iskusnykh, I.Y., Chizhikov, V.V., et al. (2022). Unified rhombic lip origins of group 3 and group 4 medulloblastoma. Nature *609*, 1012–1020.

33. Shu, M., Hong, D., Lin, H., Zhang, J., Luo, Z., Du, Y., Sun, Z., Yin, M., Yin, Y., Liu, L., et al. (2022). Single-cell chromatin accessibility identifies enhancer networks driving gene expression during spinal cord development in mouse. Dev. Cell *57*, 2761–2775.e6.

34. Hong, D., Lin, H., Liu, L., Shu, M., Dai, J., Lu, F., Tong, M., and Huang, J. (2023). Complexity of enhancer networks predicts cell identity and disease genes revealed by single-cell multi-omics analysis. Brief. Bioinform. *24*, bbac508.

35. Huang, J., Li, K., Cai, W., Liu, X., Zhang, Y., Orkin, S.H., Xu, J., and Yuan, G.C. (2018). Dissecting super-enhancer hierarchy based on chromatin interactions. Nat. Commun. *9*, 943.

36. Kaur, R., Aiken, C., Morrison, L.C., Rao, R., Del Bigio, M.R., Rampalli, S., and Werbowetski-Ogilvie, T. (2015). OTX2 exhibits cell-context-dependent effects on cellular and molecular properties of human embryonic neural precursors and medulloblastoma cells. Dis. Model. Mech. *8*, 1295–1309.

37. Splinter, E., and de Laat, W. (2011). The complex transcription regulatory landscape of our genome: control in three dimensions. EMBO J. *30*, 4345–4355.

38. Luo, Z., Xia, M., Shi, W., Zhao, C., Wang, J., Xin, D., Dong, X., Xiong, Y., Zhang, F., Berry, K., et al. (2022). Human fetal cerebellar cell atlas informs medulloblastoma origin and oncogenesis. Nature *612*, 787–794.

39. Kanchan, R.K., Perumal, N., Atri, P., Chirravuri Venkata, R., Thapa, I., Klinkebiel, D.L., Donson, A.M., Perry, D., Punsoni, M., Talmon, G.A., et al. (2020). MiR-1253 exerts tumor-suppressive effects in medulloblastoma via inhibition of CDK6 and CD276 (B7-H3). Brain Pathol. *30*, 732–745.

40. Li, X., Yue, X., Pastor, W.A., Lin, L., Georges, R., Chavez, L., Evans, S.M., and Rao, A. (2016). Tet proteins influence the balance between neuroectodermal and mesodermal fate choice by inhibiting Wnt signaling. Proc. Natl. Acad. Sci. USA *113*, E8267–E8276.

41. Xu, Y., Xu, C., Kato, A., Tempel, W., Abreu, J.G., Bian, C., Hu, Y., Hu, D., Zhao, B., Cerovina, T., et al. (2012). Tet3 CXXC domain and dioxygenase activity cooperatively regulate key genes for Xenopus eye and neural development. Cell *151*, 1200–1213.

42. Li, Y., Li, Z., Wang, C., Yang, M., He, Z., Wang, F., Zhang, Y., Li, R., Gong, Y., Wang, B., et al. (2023). Spatiotemporal transcriptome atlas reveals the regional specification of the developing human brain. Cell *186*, 5892–5909.e22.

43. Chua, G.N.L., Wassarman, K.L., Sun, H., Alp, J.A., Jarczyk, E.I., Kuzio, N.J., Bennett, M.J., Malachowsky, B.G., Kruse, M., and Kennedy, A.J. (2019). Cytosine-Based TET Enzyme Inhibitors. ACS Med. Chem. Lett. *10*, 180–185.

44. Lv, H., Catarino, J., Li, D., Liu, B., Gao, X.B., Horvath, T.L., and Huang, Y. (2023). A small-molecule degrader of TET3 as treatment for anorexia nervosa in an animal model. Proc. Natl. Acad. Sci. USA *120*, e2300015120.

45. Forster, V., Signorell, R.D., Roveri, M., and Leroux, J.C. (2014). Liposome-supported peritoneal dialysis for detoxification of drugs and endogenous metabolites. Sci. Transl. Med. *6*, 258ra141.

46. Jin, Y., Zhang, J., Xing, J., Li, Y., Yang, H., Ouyang, L., Fang, Z., Sun, L., Jin, B., Huang, P., et al. (2024). Multicellular 3D bioprinted human gallbladder carcinoma forin vitromimicry of tumor microenvironment and intratumoral heterogeneity. Biofabrication *16*.

47. Xu, Y., Sun, X., Zhang, R., Cao, T., Cai, S.Y., Boyer, J.L., Zhang, X., Li, D., and Huang, Y. (2020). A Positive Feedback Loop of TET3 and TGF-β1 Promotes Liver Fibrosis. Cell Rep. *30*, 1310–1318.e5.

48. Kreibich, E., Kleinendorst, R., Barzaghi, G., Kaspar, S., and Krebs, A.R. (2023). Single-molecule footprinting identifies context-dependent regulation of enhancers by DNA methylation. Mol. Cell *83*, 787–802.e9.

49. Suzuki, M., Liao, W., Wos, F., Johnston, A.D., DeGrazia, J., Ishii, J., Bloom, T., Zody, M.C., Germer, S., and Greally, J.M. (2018). Whole-genome bisulfite sequencing with improved accuracy and cost. Genome Res. *28*, 1364–1371.

50. Zhao, S.G., Chen, W.S., Li, H., Foye, A., Zhang, M., Sjöström, M., Aggarwal, R., Playdle, D., Liao, A., Alumkal, J.J., et al. (2020). The DNA methylation landscape of advanced prostate cancer. Nat. Genet. *52*, 778–789.

51. Klughammer, J., Kiesel, B., Roetzer, T., Fortelny, N., Nemc, A., Nenning, K.H., Furtner, J., Sheffield, N.C., Datlinger, P., Peter, N., et al. (2018). The DNA methylation landscape of glioblastoma disease progression shows extensive heterogeneity in time and space. Nat. Med. *24*, 1611–1624.

52. Han, F., Jiang, X., Li, Z.M., Zhuang, X., Zhang, X., Ouyang, W.M., Liu, W.B., Mao, C.Y., Chen, Q., Huang, C.S., et al. (2020). Epigenetic Inactivation of SOX30 Is Associated with Male Infertility and Offers a Therapy Target for Non-obstructive Azoospermia. Mol. Ther. Nucleic Acids *19*, 72–83.

53. Johnson, M.D., Mueller, M., Adamowicz-Brice, M., Collins, M.J., Gellert, P., Maratou, K., Srivastava, P.K., Rotival, M., Butt, S., Game, L., et al. (2014). Genetic analysis of the cardiac methylome at single nucleotide resolution in a model of human cardiovascular disease. PLoS Genet. *10*, e1004813.

54. Li, J., Zhao, S., Lee, M., Yin, Y., Li, J., Zhou, Y., Ballester, L.Y., Esquenazi, Y., Dashwood, R.H., Davies, P.J.A., et al. (2020). Reliable tumor detection by whole-genome methylation sequencing of cell-free DNA in cerebrospinal fluid of pediatric medulloblastoma. Sci. Adv. *6*, eabb5427.

55. Joshi, K., Liu, S., Breslin S J, P., and Zhang, J. (2022). Mechanisms that regulate the activities of TET proteins. Cell. Mol. Life Sci. *79*, 363.

56. Keyvani, V., Farshchian, M., Esmaeili, S.A., Yari, H., Moghbeli, M., Nezhad, S.R.K., and Abbaszadegan, M.R. (2019). Ovarian cancer stem cells and targeted therapy. J. Ovarian Res. *12*, 120.

57. Herrmann, A., Lahtz, C., Song, J., Aftabizadeh, M., Cherryholmes, G.A., Xin, H., Adamus, T., Lee, H., Grunert, D., Armstrong, B., et al. (2020). Integrin α6 signaling induces STAT3-TET3-mediated hydroxymethylation of genes critical for maintenance of glioma stem cells. Oncogene *39*, 2156–2169.

58. Wu, X., and Zhang, Y. (2017). TET-mediated active DNA demethylation: mechanism, function and beyond. Nat. Rev. Genet. *18*, 517–534.

59. López-Moyado, I.F., Ko, M., Hogan, P.G., and Rao, A. (2024). TET Enzymes in the Immune System: From DNA Demethylation to Immunotherapy, Inflammation, and Cancer. Annu. Rev. Immunol. *42*, 455–488.

60. Zhang, J., Chen, S., Zhang, D., Shi, Z., Li, H., Zhao, T., Hu, B., Zhou, Q., and Jiao, J. (2016). Tet3-Mediated DNA Demethylation Contributes to the Direct Conversion of Fibroblast to Functional Neuron. Cell Rep. *17*, 2326–2339.

61. Weirath, N.A., Hurben, A.K., Chao, C., Pujari, S.S., Cheng, T., Liu, S., and Tretyakova, N.Y. (2022). Small Molecule Inhibitors of TET Dioxygenases: Bobcat339 Activity Is Mediated by Contaminating Copper(II). ACS Med. Chem. Lett. *13*, 792–798.

62. Kanasty, R., Dorkin, J.R., Vegas, A., and Anderson, D. (2013). Delivery materials for siRNA therapeutics. Nat. Mater. *12*, 967–977.

63. Massagué, J., and Sheppard, D. (2023). TGF-β signaling in health and disease. Cell *186*, 4007–4037.

64. Ferrucci, V., de Antonellis, P., Pennino, F.P., Asadzadeh, F., Virgilio, A., Montanaro, D., Galeone, A., Boffa, I., Pisano, I., Scognamiglio, I., et al. (2018). Metastatic group 3 medulloblastoma is driven by PRUNE1 targeting NME1-TGF-β-OTX2-SNAIL via PTEN inhibition. Brain *141*, 1300–1319.

65. Khang, M., Lee, J.H., Lee, T., Suh, H.W., Lee, S., Cavaliere, A., Rushing, A., Geraldo, L.H., Belitzky, E., Rossano, S., et al. (2023). Intrathecal delivery of nanoparticle PARP inhibitor to the cerebrospinal fluid for the treatment of metastatic medulloblastoma. Sci. Transl. Med. *15*, eadi1617.

66. Hao, Y., Hao, S., Andersen-Nissen, E., Mauck, W.M., 3rd, Zheng, S., Butler, A., Lee, M.J., Wilk, A.J., Darby, C., Zager, M., et al. (2021). Integrated analysis of multimodal single-cell data. Cell *184*, 3573–3587.e29.

67. Chen, Y., Chen, Y., Shi, C., Huang, Z., Zhang, Y., Li, S., Li, Y., Ye, J., Yu, C., Li, Z., et al. (2018). SOAPnuke: a MapReduce acceleration-supported software for integrated quality control and preprocessing of high-throughput sequencing data. GigaScience *7*, 1–6.

68. Jühling, F., Kretzmer, H., Bernhart, S.H., Otto, C., Stadler, P.F., and Hoffmann, S. (2016). metilene: fast and sensitive calling of differentially methylated regions from bisulfite sequencing data. Genome Res. *26*, 256–262.

69. Subramanian, A., Tamayo, P., Mootha, V.K., Mukherjee, S., Ebert, B.L., Gillette, M.A., Paulovich, A., Pomeroy, S.L., Golub, T.R., Lander, E.S., and Mesirov, J.P. (2005). Gene set enrichment analysis: a knowledge-based approach for interpreting genome-wide expression profiles. Proc. Natl. Acad. Sci. USA *102*, 15545–15550.

70. Shi, Q., Liu, S., Kristiansen, K., and Liu, L. (2022). The FASTQ+ format and PISA. Bioinformatics *38*, 4639–4642.

71. Young, M.D., and Behjati, S. (2020). SoupX removes ambient RNA contamination from droplet-based single-cell RNA sequencing data. GigaScience *9*, giaa151.

72. McGinnis, C.S., Murrow, L.M., and Gartner, Z.J. (2019). DoubletFinder: Doublet Detection in Single-Cell RNA Sequencing Data Using Artificial Nearest Neighbors. Cell Syst. *8*, 329–337.e4.

73. Duttke, S.H., Chang, M.W., Heinz, S., and Benner, C. (2019). Identification and dynamic quantification of regulatory elements using total RNA. Genome Res. *29*, 1836–1846.

74. Langmead, B., Wilks, C., Antonescu, V., and Charles, R. (2019). Scaling read aligners to hundreds of threads on general-purpose processors. Bioinformatics *35*, 421–432.

75. Thorvaldsdóttir, H., Robinson, J.T., and Mesirov, J.P. (2013). Integrative Genomics Viewer (IGV): high-performance genomics data visualization and exploration. Brief. Bioinform. *14*, 178–192.

76. Yu, G., Wang, L.G., and He, Q.Y. (2015). ChIPseeker: an R/Bioconductor package for ChIP peak annotation, comparison and visualization. Bioinformatics *31*, 2382–2383.

77. Tu, S., Li, M., Chen, H., Tan, F., Xu, J., Waxman, D.J., Zhang, Y., and Shao, Z. (2021). MAnorm2 for quantitatively comparing groups of ChIP-seq samples. Genome Res. *31*, 131–145.

78. Ramírez, F., Ryan, D.P., Grüning, B., Bhardwaj, V., Kilpert, F., Richter, A.S., Heyne, S., Dündar, F., and Manke, T. (2016). deepTools2: a next generation web server for deep-sequencing data analysis. Nucleic Acids Res. *44*, W160–W165.

79. Durand, N.C., Robinson, J.T., Shamim, M.S., Machol, I., Mesirov, J.P., Lander, E.S., and Aiden, E.L. (2016). Juicebox Provides a Visualization System for Hi-C Contact Maps with Unlimited Zoom. Cell Syst. *3*, 99–101.

80. Li, B., and Dewey, C.N. (2011). RSEM: accurate transcript quantification from RNA-Seq data with or without a reference genome. BMC Bioinf. *12*, 323.

81. Bailey, T.L. (2011). DREME: motif discovery in transcription factor ChIP-seq data. Bioinformatics *27*, 1653–1659.

82. Chen, S., Zhou, Y., Chen, Y., and Gu, J. (2018). fastp: an ultra-fast all-in-one FASTQ preprocessor. Bioinformatics *34*, i884–i890.

83. Sun, J., Su, M., Ma, J., Xu, M., Ma, C., Li, W., Liu, R., He, Q., and Su, Z. (2023). Cross-platform comparisons for targeted bisulfite sequencing of MGISEQ-2000 and NovaSeq6000. Clin. Epigenetics *15*, 130.

84. Grant, C.E., Bailey, T.L., and Noble, W.S. (2011). FIMO: scanning for occurrences of a given motif. Bioinformatics *27*, 1017–1018.

85. Liu, H., Sun, Y., Zhang, Q., Jin, W., Gordon, R.E., Zhang, Y., Wang, J., Sun, C., Wang, Z.J., Qi, X., et al. (2021). Pro-inflammatory and proliferative microglia drive progression of glioblastoma. Cell Rep. *36*, 109718.

CellPress
OPEN ACCESS

STAR★METHODS

KEY RESOURCES TABLE

REAGENT or RESOURCE	SOURCE	IDENTIFIER
Antibodies		
Rabbit monoclonal anti-Ki-67	Abcam	Cat# ab15580; RRID: AB_443209
Rabbit monoclonal anti-NeuN	Abcam	Cat# ab177487; RRID: AB_2532109
Chicken monoclonal anti-SOX2	Abcam	Cat# ab171380; RRID: AB_2732072
Chicken monoclonal anti-MMP9	Santa Cruz	Cat# sc-13520; RRID: AB_627961
Rabbit monoclonal anti-OTX2	Abcam	Cat# ab183951; RRID: AB_3076432
Rabbit Polyclonal anti-TET3	Abcam	Cat# ab153724;
Rabbit monoclonal anti-EOMES	Abcam	Cat# ab183991; RRID: AB_2721040
Rabbit monoclonal anti-PBX3	Abcam	Cat# ab109173; RRID: AB_10858991
Chicken polyclonal anti-Cy5	Thermo Fisher Scientific	Cat# 700-110-098; RRID: AB_
Rabbit monoclonal anti-GAPDH	Sigma-Aldrich	Cat# G9545; RRID: AB_796208
Rabbit monoclonal anti-Smad2	Cell Signal Tech	Cat# mAB5339; RRID: AB_10626777
Rabbit monoclonal anti-*p*-Smad2	Cell Signal Tech	Cat# mAB8828; RRID: AB_2631089
Goat monoclonal anti-TGF-β1	Cell Signal Tech	Cat# mAB3711; RRID: AB_2063354
Rabbit monoclonal anti-TβRII	Cell Signal Tech	Cat# mAB41896; RRID: AB_3668871
Bacterial and virus strains		
pMD2.G (VSV-G envelope)	Addgene	Cat# 12259
psPAX2	Addgene	Cat# 12260
pRL-SV40P	Addgene	Cat# 27163
Biological samples		
Human medulloblastoma tissue	Capital Medical University Beijing Titantan Hospital	N/A
PDX xenografts	This study	N/A
Chemicals, peptides, and recombinant proteins		
TET3 inhibitor (Bobcat339)	MCE	Cat# HY-111558
Minocycline	Sigma-Aldrich	Cat# M9511
Neurobasal	ThermoFisher Scientific	Cat# 21103049
DMEM/F12	GIBCO	Cat# 11320033
FBS	ThermoFisher Scientific	Cat# 10099
Pepsin	Sigma-Aldrich	P7000
B27	Invitrogen	Cat# 12587010
bFGF	Stemcell Tech	Cat# 78003
EGF	Stemcell Tech	Cat# 78006
Penicillin/Streptomycin	GIBCO	Cat# 15140163
L-glutamine	GBICO	Cat# 25030149
Collagenase type IV	Sigma-Aldrich	Cat# 11088866001
DNase I	ThermoFisher Scientific	Cat# EN0521
BSA	Sigma-Aldrich	Cat# A3059
Betaine solution	Sigma-Aldrich	Cat# B0300
Phosphatase inhibitor	ThermoFisher Scientific	Cat# 1862495
Protease inhibitor	ThermoFisher Scientific	Cat# 1861278
iScript_ Reverse Transcription Supermix	Bio-rad Inc.	Cat# 170-8841
TRIzol reagent	ThermoFisher Scientific	Cat# 15596018
SYBR Green PCR Master Mix	Qiagen	CAS# 330501

(*Continued on next page*)

Continued

REAGENT or RESOURCE	SOURCE	IDENTIFIER
Red Blood Cell Lysis Buffer	Sigma-Aldrich	Cat# 11814389001
dNTP Mix (10 mM)	ThermoFisher Scientific	Cat# R0192
Minocycline	Sigma-Aldrich	Cat# M9511
Critical commercial assays		
Brain Tumor Dissociation Kit	Miltenyi Biotech	Cat# 130-095-942
Dead Cell Removal Kit	Miltenyi Biotech	Cat# 130090101
Transwell Kit	ThermoFisher Scientific	Cat# 140627
FISH Kit	Abcam	Cat# ab253402
Multivision Polymer Detection system	Lab Vision	Cat# TL-012-MARH
Brain Tumor Dissociation Kit	Miltenyi Biotech	Cat# 130-095-942
Dead Cell Removal Kit	Miltenyi Biotech	Cat# 130090101
Transwell Kit	ThermoFisher Scientific	Cat# 140627
FISH Kit	Abcam	Cat# ab253402
Deposited data		
Tumor whole-genome bisulfite sequencing (WGBS) data of MB	This study	CNGB: CNP0005827
Tumor single-nucleus RNA and ATAC-seq data of MB	This study	CNGB: CNP0006024
Bulk tumor RNA-seq data of MB	This study	CNGB: CNP0006024
CUT&Tag-seq data of D283	This study	CNGB: CNP0006023
OTX2 ChIP-seq data of D283 & D341	Boulay et al.[18]	GEO: GSE92585
Hi-C data of MB004	Luo et al.[37]	GEO: GSE198565
Methylation & expression profiling by array of MB	Cavalli et al.[2]	GEO: GSE85217
Experimental models: Cell lines		
Human: MB tumor cells	This study	N/A
Human: HK293T/17	ATCC	CRL-12688
Human: D283	ATCC	HTB-185
Human: D458	Shanghai Jiao Tong University College	N/A
Experimental models: Organisms/strains		
Mouse: C57/BL6 wild type	Beijing Vitalriver Lab	N/A
Rat: SRG Rat	Beijing Vitalriver Lab	N/A
Oligonucleotides		
siTET3-1: GUCCUGGGUUCCAAGACAATT (sense 5–3), UUGUCUUGGAACCCAGGACTT (antisense 5–3); siTET3-2: GUGUCCUCCUAUGCCUACATT (sense 5–3), UGUAGGCAUAGGAGGACACTT (antisense 5–3); siTET3-3: CUACGGUGGUGCUGAGUUUTT (sense 5–3), AAACUCAGCACCACCGUAGTT (antisense 5–3).	This study	N/A
Software and algorithms		
R v4.4.2	N/A	https://www.r-project.org/
Seurat v4.4.0	Hao et al.[66]	https://github.com/satijalab/seurat
SOAPnuke v2.1.8	Chen et al.[67]	https://github.com/BGI-flexlab/SOAPnuke
BitMapperBS v1.0.2.3	N/A	https://github.com/chhylp123/BitMapperBS
MarkDuplicates (Picard)	GATK	https://github.com/broadinstitute/gatk
MethylDackel v0.6.1	N/A	https://github.com/dpryan79/MethylDackel
SNFtool v2.3.1	N/A	https://github.com/maxconway/SNFtool
Metilene v0.2.8	Jühling et al.[68]	http://legacy.bioinf.uni-leipzig.de/Software/metilene/

(*Continued on next page*)

Continued

REAGENT or RESOURCE	SOURCE	IDENTIFIER
GenomicRanges 1.58.0	N/A	https://github.com/Bioconductor/GenomicRanges
Igraph 2.1.4	N/A	https://igraph.org/
RSpectra 0.16.2	N/A	https://github.com/yixuan/RSpectra
CNVpytor v1.3.1	N/A	https://github.com/abyzovlab/CNVpytor
GSEA	Subramanian et al.[69]	https://www.gsea-msigdb.org/gsea/index.jsp
FIMO (MEME Suite)	N/A	https://meme-suite.org/meme/doc/fimo.html
PISA v1.3	Shi et al.[70]	https://github.com/shiquan/PISA
SoupX 1.6.2	Young et al.[71]	https://github.com/constantAmateur/SoupX
DoubletFinder 2.0.6	McGinnis et al.[72]	https://github.com/chris-mcginnis-ucsf/DoubletFinder
HOMER v5.1	Duttke et al.[73]	http://homer.ucsd.edu/homer/
Bowtie2 v2.5.4	Langmead et al.[74]	https://github.com/BenLangmead/bowtie2
SEACR v1.4	N/A	https://github.com/FredHutch/SEACR
IGV 2.16.0	Thorvaldsdóttir et al.[75]	https://igv.org/
ChIPseeker	Yu et al.[76]	https://github.com/YuLab-SMU/ChIPseeker
Manorm	Tu et al.[77]	https://manorm.readthedocs.io/en/latest/
Deeptools 3.5.5	Ramírez et al.[78]	https://github.com/deeptools/deepTools
Juicebox v2.20.00	Durand et al.[79]	https://github.com/aidenlab/Juicebox
RSEM v1.3.3	Li et al.[80]	https://github.com/deweylab/RSEM
MEME Suite/DREME	Bailey.[81]	https://web.mit.edu/meme/current/share/doc/meme.html
fastp v0.24.0	Chen et al.[82]	https://github.com/OpenGene/fastp

EXPERIMENTAL MODEL AND SUBJECT DETAILS

Patients and samples

Primary MB samples were obtained from 190 chemo-/radiotherapy-naïve patients undergoing craniotomy from December 2010 to July 2023 at Beijing Tiantan Hospital, Capital Medical University (Beijing, China). Written informed consent was obtained from patients or guardians for tissue collection following approval from the Research Ethics Committee of Beijing Tiantan Hospital, Capital Medical University, and the Institutional Review Board of Beijing Genomics Institute-Shenzhen (BGI-IRB; KY2022-133-03 and KY2023-130-01). To protect patient identities, samples were coded and distributed by patient ID.

Cells

The human MB D283 and D458 cell lines were obtained from Shanghai Jiao Tong University College of Basic Medical Sciences (Shanghai, China) in June 2022. Cells at passage C4 before thawing were confirmed to be free of mycoplasma contamination via PCR. Species origin was confirmed by PCR, with results accessible on an official website (http://cellresource.cn). Identity was authenticated with STR profiling (FBI, CODIS) before cryopreservation or withdrawal of vials from a lot for examination.

Experimental animal sourcing and housing

Six-to-eight-week-old C57BL/6 wild-type mice or SCID mice and immunodeficient rats were purchased from Beijing Vitalstar Biotechnology Co., Ltd. (Beijing, China). All animals were housed at the Laboratory Animal Facility of Beijing Neurosurgical Institute (Beijing, China). Animal experiments were approved by the Animal Care Committee and performed in accordance with national guidelines. Sex as a biological variable. Both male and female human samples were included for sequencing profiles. For all mouse or rat studies, male and female animals were included. Sex was not considered as a biological variable in the statistical analyses.

Mouse models of G3-MB

Dissociated D283 or D458 cells infected with shOTX2 or nontarget shRNA (1×10^7 cells/mL) were subcutaneously injected into the left flank of six-to eight-week-old Bal-B/C nude mice ($n = 6$/group). Tumor volume was measured every 2 days and calculated via the following formula: V (mm^3) = 1/2 ($L \times W^2$). After 4 weeks, the mice were sacrificed, and the tumor sections were stained with the corresponding antibodies.

Additionally, infected D283 or D458 cells (1×10^6 cells/mL) were used for intracranial injection into the right cerebellar hemisphere via a mouse stereotaxic apparatus as described previously[12,16]. Briefly, SCID mice (n = 3/group) anesthetized with ketamine (100 mg/kg) plus xylazine (9 mg/kg) were positioned on a stereotaxic frame. An incision was made in the midline of skull over the right cerebellum. A 24-G Hamilton syringe loaded with cells was mounted on a micromanipulator and introduced through the hole at a 90° angle to cerebellum at 2.0 mm. The available cells were intracranially injected over 2 min with a needle for an additional 2 min.

Human G3-MB tumor tissues collected during operations were minced within 30 min, and then injected into the right cerebellar hemisphere of immunodeficient rats via a stereotaxic apparatus (n = 6/group). Then, microMRI scanning was conducted on the 7th ~ 10th day post-injection to monitor tumor growth. Survival was measured from transplantation until death. Rats were sacrificed and tumor sections were stained with the corresponding antibodies.

METHOD DETAILS

WGBS data processing

To measure the efficiency of bisulfite conversion, DNA was extracted and WGBS libraries were prepared, incorporating 0.5% λ phage DNA as an unmethylated control. The efficiency of bisulfite conversion, as indicated by the λ phage DNA spike-in, exceeded 99.5% in all medulloblastoma samples. Using a Covaris M220 focused ultrasonicator, the samples were fragmented to a mean size of 250 bp. The EZ DNA Methylation-Gold Kit was utilized for bisulfite conversion, whereas the Accel-NGS Methyl-Seq Kit was employed for library construction. The quality of the libraries was evaluated using 2100 Bioanalyzer. Sequencing was performed at the sequencing core facility, utilizing the MGISEQ-2000 system to generate paired-end reads with a length of 151 bp.[83]

The raw sequencing data were subjected to quality control via SOAPnuke[67] to filter out reads on the basis of quality thresholds and adapter contamination. Specifically, adapter sequences AAGTCGGAGGCCAAGCGGTCTTAGGAAGACAA and AAGTCGGATCG TAGCCATGTCGTTCTGTGAGCCAAGGAGTTG were removed, with nondefault parameters set to -n 0.1. Subsequently, the filtered reads were aligned to the human reference genome (hg38) via BitMapperBS (version_1.0.2.3). PCR duplicates were identified and removed via Picard MarkDuplicates. Finally, MethylDackel (version_0.6.1) was utilized to extract and quantify cytosine methylation levels from the processed sequencing data.

Bulk gene expression profiling

Human MB sample RNA sequencing profiles were obtained using BGISEQ-50 platform (Shenzhen, China). The sequencing reads obtained were aligned to the hg38 genome, and the quantification of gene expression was conducted using RNA-Seq by Expectation-Maximization (RSEM) software,[80] thereby establishing a raw count matrix. Subsequently, the count data were normalized to transform them into transcripts per million (TPM) values. All subsequent analyses were conducted using these TPM values, providing a normalized and comparable metric for gene expression across samples.

Unsupervised molecular subgroup analysis

In both discovery and validation cohorts, differential methylation analysis compared tumor tissues to normal cerebellar tissues, aiming to identify DMRs. The top 25% of the most variable DMRs were selected for principal component analysis (PCA). Pairwise probe covariance of DMR β-values was computed, followed by eigenvalue decomposition via the eigs function of the RSpectra package. The number of principal components was determined by comparing eigenvalues to the maximum eigenvalue of PCA using randomized β values (DMR random matching across different samples). These principal components were then used for t-SNE analysis with the following parameters: theta = 0, pca = F, max_iter = 2500, perplexity = 10.

G3-MB subtype identification

Subtype classification was achieved by employing similarity network fusion (SNF), as outlined in previous studies,[2] utilizing RNA-seq expression data and average methylation levels of gene promoters instead of microarray data. Comprehensive expression and methylation datasets were fed into the SNF function within the R package SNFtool (v_2.3.1). The parameters set for this analysis included K = 15, α = 0.5, and T = 100. Spectral clustering was subsequently executed, resulting in clusters at k = 3, which matched three G3 subtypes.

DMRs analysis and annotation

DMR analysis was conducted using metilene(v0.2.8)[68] with the following nondefault parameter settings: -m 8 -Y 0.75 -M100. DMRs with a q value < 0.05 were selected. Gene annotations for hg38 and CpG islands were obtained from the UCSC Genome Browser. Promoters were defined as regions extending 1500 bp upstream to 500 bp downstream of the transcription start site (TSS). Enhancer annotation files were derived from previously published H3K27ac ChIP-seq data for MB. Subsequently, the 'findOverlaps' function in the GenomicRanges R package was used to annotate DMRs as bDMR, seDMR, pDMR, and CGI, targeted genes were assigned to DMRs.

Identification of functional differentially methylated regions (F-DMRs)

F-DMRs are defined by a significant correlation between methylation levels and the expression levels of their target genes. Specifically, F-seDMRs and F-pDMRs were identified with a significant negative correlation (Spearman analysis, $p < 0.05$), indicating an inverse relationship between methylation and gene expression.

CNV analysis

Chromosomal arm-level CNV analysis was performed on the methylation sequencing alignment files using CNVpytor. The bin size was set to 50,000. A custom reference genome was utilized, involving C to T and G to A conversions in the reference genome hg38.

Gene set enrichment analysis

Enrichment analysis was performed for target genes of seDMRs, pDMRs, and bDMRs using Fisher's exact test. Reference gene signature sets comprised marker genes of various cell types during cerebellar development, including RL^{VZ}, RL^{SVZ}, early UBCs, late UBCs, early GN, and GN. Results were adjusted for multiple reference gene sets via Benjamini-Hochberg (BH) correction.

Otx2 SEs methylation-dependent differentiation potential

We stratified tumors into OTX2 super-enhancer (SE) hyper- and hypomethylation groups based on median methylation level. Differential methylation analysis integrated with gene set enrichment analysis (GSEA)[69] was performed using the late-stage urothelial basal cell/glandular neoplastic (Late UBC/GN) signature as the terminal differentiation gene set.

Construction of single-gene enhancer networks

We extracted peaks overlapping with enhancers from snATAC-seq data and utilized the eNet algorithm to construct enhancer networks for individual genes.[33,34] Upon obtaining the enhancer networks for each gene, the 'cluster_edge_betweenness' function from the igraph R package was used to divide the networks into distinct subnetworks. We define 'hub enhancers' as enhancers within the subnetwork that includes the enhancer identified as the 'most central' using 'community_edge_betweenness' function in R package igraph (version_2.1.4) for degree centrality. All other enhancers are classified as 'non-hub enhancers'. Consequently, F-seDMRs overlapping with 'hub enhancers' are termed 'hub F-seDMRs'.

Otx2 enhancer interaction network analysis

We conducted a scan for *Otx2* motifs within all enhancer regions using FIMO (https://meme-suite.org/meme/),[84] identifying enhancers with OTX2 binding sites. For enhancers where targeted gene is a transcription factor, this process was repeated. We hypothesized that these transcription factors, regulated by OTX2, further influenced a broader transcriptional network, leading to the identification of an OTX2-regulated enhancer network.

snRNA-seq suspension preparation

Single-nucleus suspensions were prepared according to established protocols.[85] Frozen tissue samples were thawed and finely chopped before being introduced into a 1 mL Dounce homogenizer along with 1 mL of homogenization buffer A. This specialized buffer comprised 250 mM sucrose, 10 mg/mL bovine serum albumin, 5 mM $MgCl_2$, 0.12 U/μL RNasin Plus, and 1× cOmplete protease inhibitor cocktail, and the mixture was kept on ice throughout the process. Homogenization was performed with a loose pestle (Pestle A) for 25 strokes, after which the homogenate was strained through a 100 μM cell strainer. The strained mixture was then transferred to a fresh homogenizer containing 750 μL of buffer A supplemented with 1% IGEPAL. Further homogenization with a tight pestle (Pestle B) for 25 strokes ensued, followed by straining through a 40 μm strainer into a 1.5 mL tube. Centrifugation at 500*g* for 5 min at 4°C facilitated nuclear sedimentation. The sedimented nuclei were reconstituted in 1 mL of buffer B, composed of 320 mM sucrose, 10 mg/mL bovine serum albumin, 3 mM $CaCl_2$, 2 mM magnesium acetate, 0.1 mM EDTA, 10 mM Tris-HCl, 1 mM dithiothreitol (DTT), 0.12 U/μL RNase, and 1× cOmplete Protease Inhibitor Cocktail, followed by another centrifugation step under identical conditions to pellet the nuclei. Finally, the nuclei were resuspended in cell resuspension buffer to achieve a concentration of 1,000 nuclei/μL for subsequent library preparation.

snRNA-seq library preparation

We utilized the DNBelab C Series Single-Cell Library Prep Set (1000021082; MGI, Shenzhen, China), following established methodologies. This procedure encompassed the processing of single-nucleus suspensions across several stages: droplet generation, emulsion disruption, bead collection, reverse transcription, and cDNA amplification, resulting in the generation of barcoded libraries. Quantification of library concentrations was performed via a Qubit single-stranded DNA (ssDNA) Assay Kit (Cat#Q10212; Thermo Fisher Scientific). Sequencing was conducted on DNBSEQ-T1/-T7 sequencers located at the China National Gene Bank (CNGB, Shenzhen, China), adhering to a sequencing protocol featuring a 30-bp read length for Read 1 and a 100-bp read length for Read 2.

snRNA-seq data processing

For raw data processing, sequencing reads from DNBSEQ-T1/-T7 sequencers were filtered and demultiplexed via PISA (version_1.3).[70] Considering the presence of unprocessed pre-mRNAs in nuclear samples, a specific "pre-mRNA" reference was

constructed, encompassing both exon and intron reads. This strategy enabled the calculation of transcript counts for each gene by aggregating exon and intron reads, yielding a unique molecular identifier (UMI) count matrix across nuclei and genes generated with PISA.

Ambient RNA mitigation

SoupX[71] was applied using standard settings, with exception of adjusting the contamination fraction (Rho). In instances where Rho was less than 0.05 or greater than 0.2, the autoEstCont function was utilized to automatically fine-tune this parameter. For samples exhibiting Rho values within the range of 0.05–0.2, the contamination fraction was manually set to 0.2 via the 'setContaminationFraction' function, to ensure optimal noise reduction.

Doublet exclusion

To eliminate doublets, DoubletFinder[72] was applied to each library individually. With the default settings, the top 5% of nuclei most resembling pseudo-doublets were identified and subsequently removed from the dataset.

snATAC-seq data processing

The snATAC-seq libraries were prepared via the DNBelab C Series Single-Cell ATAC Library Prep Set70 (1000021878; MGI, China) following established protocols. Initially, nuclei were isolated from frozen tissue samples, as described in prior studies. Subsequently, Tn5 tagmentation was applied to the isolated nuclei, followed by processing to generate barcoded snATAC-seq libraries. This process involved droplet encapsulation, preamplification, emulsion breakage, bead capture and collection, DNA amplification, and purification. Library concentrations were quantified using the Qubit ssDNA Assay Kit. Sequencing was performed on the BGISEQ-500 sequencer at the CNGB, utilizing a sequencing format comprising a 50-bp read length for Read 1 and a 76-bp read length for Read 2.

We processed by processing the raw sequencing reads from the BGISEQ-500 platform. These reads underwent a filtering and demultiplexing process, followed by alignment to the human hg38 genome using PISA software. This alignment facilitated the generation of fragment files, which served as the basis for subsequent analyses.

Cell clustering and cell-type identification in snRNA-seq dataset

To secure high-quality data for further analysis, we filtered the snRNA-seq data, setting a minimum expression threshold of 500 genes per nucleus, with each gene needing expression in at least three nuclei. Nuclei with more than 20% mitochondrial gene counts were excluded. After filtering, the data were logarithmically transformed by ln (counts per million/100 + 1). We selected 3,000 genes exhibiting high variability based on their average expression and dispersion. The number of UMIs and the proportion of mitochondrial genes were adjusted for, and genes were scaled using the default settings. We used Seurat (v_4.4.0)[66] for global clustering of the entire tumor tissue dataset, with manual fine-tuning of parameters for optimal cell clustering.

To discern cellular subpopulations, we conducted principal component analysis on the snRNA-seq data for dimensional reduction and employed the Louvain algorithm to uncover community structures. In the process of clustering individual tissues, we utilized the Seurat package (v_4.4.0)[66] within R (v_4.4.2). We normalized data from various replicates and identified the top 2,000 highly variable genes from each replicate via the 'FindVariableFeatures' function with the vst method. For batch correction, replicable variable genes were chosen using the 'FindIntegrationAnchors' function and were integrated into a unified data assay. Clustering and visualization of this integrated assay were carried out using default settings following the standard Seurat workflow. Each cluster was characterized based on distinct gene expression profiles.

Integration of snRNA-seq and snATAC-seq data

To assign cell type identities from snRNA-seq data to cells in snATAC-seq datasets, we utilized the 'TransferData' function of Seurat to establish anchors between both datasets. We conducted canonical correlation analysis to merge the log-normalized gene activity scores from snATAC-seq with the gene expression scores from snRNA-seq. This integration was facilitated by Seurat's 'FindTransferAnchors' function, taking as input the collection of the 2,000 most variable genes from both snRNA-seq and snATAC-seq datasets. Subsequently, canonical correlation analysis (CCA) was carried out using Seurat's default settings. For each cell analyzed by snATAC-seq, we searched the combined CCA L2 space to locate the closest neighboring cell from the snRNA-seq dataset. The nearest neighbors were determined using the 'FNN' R package and the 'kd_tree' algorithm.

Identification of DEGs and GO enrichment

We conducted pairwise comparisons to assess differential gene expression among subgroups, with each subgroup compared against all others, resulting in four comparisons. T-tests were utilized for analysis, with p-values adjusted via false discovery rate (FDR) correction. The heatmap displayed the top 20 upregulated protein-coding genes.

Transcription factor motif enrichment analysis

We conducted motif enrichment analysis on both hypermethylated and hypomethylated enhancer regions using the 'findMotifsGenome' function of the HOMER software.[73]

Scoring of the TGF-β-Smad signaling pathway

In bulk RNA-seq analysis, genes related to the "TGF-β receptor signaling active Smads" pathway were retrieved from KEGG database. Each sample was scored using GSVA, and subsequently divided into two groups according to the median score. For snRNA-seq, the 'AddModuleScore' function in the Seurat package was utilized to compute the pathway score for each cell.

Gene Expression Omnibus and European Genome-phenome archive data validation

CNV and bulk RNA-seq data were retrieved from Gene Expression Omnibus (GEO) and European Genome-phenome Archive (EGA) data portals, acquiring data from 567 MB cases. Each gene with $\geq$10 cases width a specific CNV pattern was included. From the available clinical data, these initial enrollments with follow-up profiles were used in the current study.

CUT&Tag-seq

CUT&Tag assay was performed using the HyperactiveTM *in situ* ChIP Library Prep Kit for Illumina (Cat#TD901-TD902, Vazyme Biotech) according to the manufacturer's instructions.[15] Concanavalin A-coated magnetic beads (ConA beads) were applied to bind D283 cells at room temperature. The cell membrane was permeabilized with digitonin, and then a TET3 antibody (Cat#PA5-31860, Thermo Fisher Scientific), secondary antibody, and hyperactive pA-Tn5 transposase were sequentially added to the ConA bead-bound cells. This process ensured precise cutting of DNA fragments bound to target protein by hyperactive pA-Tn5 transposase. The cut DNA fragments were ligated with P5 and P7 adaptors via Tn5 transposase, and libraries were PCR-amplified with the P5 and P7 primers. PCR products were assessed via an Agilent 2100 Bioanalyzer (Agilent Technologies). Finally, Illumina NovaSeq 6000 platform was employed for sequencing, generating 150 bp paired-end reads for subsequent analysis.

Raw sequencing data underwent quality trimming using fastp[82] software to yield clean reads, which were then aligned to hg38 using Bowtie2.[74] Subsequent analysis was conducted with SEACR software, employing the 'stringent' parameter to identify genomic regions enriched for multiple overlapping DNA fragments (peaks), indicating potential binding sites. Peak distribution along the genomic regions of target genes was executed using IGV[75] and annotated using ChIPseeker[76] software to obtain gene information and annotations. Significantly enriched motifs in the peaks were analyzed using MEME and DREME software and aligned with motif database.[81]

Manorm2 software [77] was used to analyze distinct peaks. Initially, the algorithm constructed a regression model involving the M-value of common peaks in the sample to mitigate the impact of sequencing deviations. The M-value was defined as the log2 value (case common peak abundance). Subsequently, p values were calculated using a Bayesian model. Finally, peaks with a p-value <0.05 and $|\text{M value}| > 1$ were deemed significantly different.

Visualization of ChIP-seq, Hi-C data and CUT&Tag-seq

All genomic regions related to ChIP-seq data in the study were visualized using IGV (v2.16.0).[75] ChIP-seq data and CUT&Tag-seq heatmaps were created using Deeptools (v3.5.5),[78] and Hi-C data heatmaps were visualized via Juicebox(v2.20.00).[79]

Reagents

Otx2 SE mutant plasmids and siTET3 were purchased from Guangzhou RiboBio Co., Ltd. (Guangzhou, China). The sequences of siRNAs targeting Tet3 were as follows: siTET3-1, GUCCUGGGUUCCAAGACAATT (sense 5–3), UUGUCUUGGAACCCAGGACTT (antisense 5–3); siTET3-2, GUGUCCUCCUAUGCCUACATT (sense 5–3), UGUAGGCAUAGGAGGACACTT (antisense 5–3); siTET3-3, CUACGGUGGUGCUGAGUUUTT (sense 5–3), AAACUCAGCACCACCGUAGTT (antisense 5–3).

Nanoparticle-loaded Bobcat339 or siRNA construction

First, 40 mg of soy lecithin, 20 mg of cholesterol, 10 mg of DSPE-MPEG2000 and 200 μL of Bobcat339 (1 mg/mL) were dissolved in 4 mL of $CHCl_3$. The solution was then rotation evaporated to remove $CHCl_3$ and form a lipid film on the inner wall of the bottom of the flask. After drying under vacuum overnight, 1 mL of ultrapure water was added to the flask. The mixture was stirred and ultrasonicated for 20 min. Then, the emulsion was extruded 20 times by a liposome extruder to obtain LNP@Bobcat339.

First, 20 mg of DLin-MC3-DMA, 20 mg of soy lecithin, 10 mg of cholesterol, and 5 mg of DSPE-MPEG2000 were dissolved in 5 mL of $CHCl_3$. The solution was then rotation evaporated to remove $CHCl_3$ and form a lipid film on the inner wall of the bottom of the flask. After drying under vacuum overnight, 1.5 mL of siRNA solution (10 μmol) was added to the flask, which was stirred and ultrasonicated for 20 min. Then, the obtained emulsion was extruded 20 times by a liposome extruder and concentrated to 150 μL via ultrafiltration.

H.&E., immunohistochemistry and immunofluorescence staining

Paraffin-embedded samples were sectioned sagittally at a thickness of 5 μm for H.&E. staining and immunostaining. Antibodies against OTX2, Ki-67, NeuN, MMP9 and TET3 were applied, and the samples were incubated at 4°C overnight. The percentage of positively stained cells was determined by counting 500 nuclei in four high-magnification (400×) representative fields. Frozen cells were initially blocked for 1 h in normal goat serum. Antibodies against SOX2, NeuN and Ki-67 were applied, and samples were incubated overnight at 4°C. The sections were subsequently stained with fluorescein isothiocyanate-labeled secondary antibodies for 1 h at room temperature. Finally, all samples were counterstained with 4′,6-diamidino-2-phenylindole.

CCK8 examination

A Cell Counting Kit-8 (CCK-8) assay was performed in D283 or D458 cells with CCK8 reagent to measure viability following the corresponding treatments. Cells were seeded in 96-well plates, incubated, and then treated with CCK8 solution. After further incubation, the absorbance was measured via a microplate reader.

Transwell assay

A migration test was conducted with Transwell chambers. In brief, D283 cells were placed in upper chambers (1×10^3 in 100 μL), while the lower chambers were supplied with 500 μL of DMEM containing 10% FBS. The reagents were added to the upper chambers. After 8 h, the filters were fixed, stained with 0.1% crystal violet, and subsequently counted.

Plasmid transfection

D283 MB cells were transfected with plasmids harboring either wild-type or mutant *Otx2* binding motifs at the E33 enhancer region using Lipofectamine 3000 (Thermo Fisher Scientific) following the manufacturer's instructions. Cells were seeded at 60–70% confluency in 6-well plates and transfected with 2 μg of plasmid DNA per well. Transfection efficiency was monitored by co-transfection with the reporter gene, and downstream assays were performed 24–48 h post-transfection. Plasmid sequences are provided in supplementary profiles.

RNA extraction and qRT–PCR

RNA was extracted from D283 and D458 cells via TRIzol reagent following the manufacturer's guidelines (Invitrogen). cDNA was subsequently synthesized from 2 μg of total RNA via iScript reverse transcription reagent. mRNA levels were quantified via SYBR Green on the Mx3000P QPCR system and normalized against the expression of GAPDH mRNA.

Cell lysis

Cell and tissue lysis was carried out using ice-cold buffer comprising 0.1% Triton X-100 and 20 mmol/L Tris-HCl (pH = 7.4) with a protease inhibitor cocktail. The protein concentration was determined via a bicinchoninic acid assay following the manufacturer's instructions (Invitrogen).

Immunoblotting analysis

The whole proteins (50 μg) were separated via a 10% SDS–PAGE gel and then transferred to PVDF membranes. These membranes were subsequently treated with anti-OTX2, anti-TET3, anti-TGF-β1, anti-TGF-βRII, anti-Smad2, anti-*p*-Smad2 and anti-GAPDH antibodies overnight at 4°C. The secondary antibodies were then applied, and the samples were probed for 1 h at room temperature. The primary antibodies were mostly diluted at 1 : 500, except for anti-GAPDH, which was diluted at 1:3000.

Co-immunoprecipitation (Co-IP)

Lysates from tumor cells (500 μg) were separately incubated overnight at 4°C with either anti-OTX2 or anti-TET3 antibodies, which were cross-linked with protein A/G beads. Protein elution from the beads was subsequently conducted, followed by electrophoresis on a 10% SDS–PAGE gel. Immunoblotting for the specified antibodies was then carried out.

ChIP–qRT–PCR

D283 cells were fixed in 4% paraformaldehyde at room temperature for 15 min. After rinsing with DPBS, cells were lysed in buffer supplemented with 1% SDS, 50 mM Tris-HCl (pH = 8.1), and 10 mM EDTA, followed by 15 min of sonication. The resulting solution was diluted in ChIP-dilution buffer. The chromatin was then incubated with an anti-TET3 antibody overnight at 4°C. Immunoprecipitates were collected utilizing protein A-Sepharose beads and washed sequentially. Elution buffer was used to release the immune complexes, and protein–DNA crosslinking was reversed. DNA was isolated, and PCR products were quantified via the CFX96 Real-Time System (Bio-Rad).

Quantitative methylation-specific PCR (qMSP)

QMSP was performed to assess the methylation level at *Otx2* enhancer region. Briefly, primers specific to methylated and unmethylated sequences within the *Otx2* enhancer region were designed. Genomic DNA was extracted from the G3-MB sample via standard procedures. Bisulfite conversion was performed on the extracted DNA to convert unmethylated cytosines to uracil while leaving methylated cytosines unchanged. PCR amplification was conducted separately via primers targeting methylated and unmethylated sequences. The amplified products were quantified via qPCR, which measured the fluorescence of DNA-binding dyes or hydrolysis probes.

Three-dimensional (3D) bioprinted MB tetra-culture models

A 3D tetra-culture model was generated using extrusion-based 3D bioprinting, as described previously.[46] Briefly, MB tissue specimens were collected immediately following resection. The tumor tissues were enzymatically dissociated into single-cell suspensions and subsequently printed using a 3D bioprinter (ALPHA-CPT1, SUNP BIOTECH). Cells were blended at defined ratios with gelatin

and sodium alginate to form concentric cylinders, consisting of an MB cell core surrounded by an outer layer containing, or lacking, stromal cells such as HUVECs, CCC-ESF-1 fibroblasts, and differentiated THP-1 macrophages. The resulting *in vitro* 3D tetra-culture constructs were then treated with reagents, and cell viability was assessed using the CCK8 assay.

Treatments in rats

We implemented catheterization in immunodeficient rats for multiple intraventricular medications without anesthesia. Nanoparticle-coated inhibitors or siRNAs targeting TET3 (LNP@Bobcat339 or LNP@siTET3) were evaluated *in vivo*. For intracranial xenografts, on the 4th day post-transplantation of dissociated G3-MB PDX tumor cells, rats with intracranial xenografts were randomly assigned to receive intraventricular treatment with LNP@Bobcat339 or LNP@siTET3 or the control (n = 6/group).

QUANTIFICATION AND STATISTICAL ANALYSIS

Data analysis was performed using R statistical environment. Error bars in bar graphs depict the standard error of the mean (SEM). Two-group comparisons were performed with the two-tailed Student's t test. For all tests, $p < 0.05$ was considered statistically significant. Asterisk denotations in figures are: $^{*}p < 0.05$, $^{**}p < 0.01$, $^{***}p < 0.001$, $^{****}p < 0.0001$. Categorical and distribution variables between entity types were compared by two-sided Fisher's exact test and Wilcoxon rank-sum test, respectively. Overall survival analysis was evaluated using Kaplan–Meier method. For all tests, a p-value < 0.05 indicated statistical significance.